Revisiting the Helium and Hydrogen Accretion Indicators at TWA 27B: Weak Mass Flow at Near-freefall Velocity

Gabriel-Dominique Marleau[1,2,3,4] , Yuhiko Aoyama[5] , Jun Hashimoto[6,7,8] , and Yifan Zhou[9]

[1] Fakultät für Physik, Universität Duisburg-Essen, Lotharstraße 1, D-47057 Duisburg, Germany; gabriel.marleau@uni-tuebingen.de, gabriel.marleau@uni-due.de
[2] Institut für Astronomie und Astrophysik, Universität Tübingen, Auf der Morgenstelle 10, D-72076 Tübingen, Germany
[3] Physikalisches Institut, Universität Bern, Gesellschaftsstr. 6, CH-3012 Bern, Switzerland
[4] Max-Planck-Institut für Astronomie, Königstuhl 17, D-69117 Heidelberg, Germany
[5] Kavli Institute for Astronomy and Astrophysics, Peking University, Beijing 100084, People's Republic of China
[6] Astrobiology Center, National Institutes of Natural Sciences, 2-21-1 Osawa, Mitaka, Tokyo 181-8588, Japan
[7] Subaru Telescope, National Astronomical Observatory of Japan, Mitaka, Tokyo 181-8588, Japan
[8] Department of Astronomy, School of Science, Graduate University for Advanced Studies (SOKENDAI), Mitaka, Tokyo 181-8588, Japan
[9] Department of Astronomy, University of Virginia, 530 McCormick Rd., Charlottesville, VA 22904, USA
Received 2023 September 27; revised 2024 January 9; accepted 2024 January 9; published 2024 March 18

Abstract

TWA 27B (2M1207b) is the first directly imaged planetary-mass ($M_\mathrm{p} \approx 5\,M_\mathrm{J}$) companion and was observed at 0.9–5.3 μm with JWST/NIRSpec. To understand the accretion properties of TWA 27B, we search for continuum-subtracted near-infrared helium and hydrogen emission lines and measure their widths and luminosities. We detect the He I triplet at 4.3σ and all Paschen-series lines covered by NIRSpec (Paα, Paβ, Paγ, Paδ) at 4σ–5σ. The three brightest Brackett-series lines (Brα, Brβ, Brγ) as well as Pfγ and Pfδ are tentative detections at 2σ–3σ. We provide upper limits on the other hydrogen lines, including on Hα through Hubble Space Telescope archival data. Three lines can be reliably deconvolved to reveal an intrinsic width $\Delta v_\mathrm{intrsc} = (67 \pm 9)\,\mathrm{km\,s^{-1}}$, which is 60% of the surface freefall velocity. The line luminosities seem significantly too high to be due to chromospheric activity. Converting line luminosities to an accretion rate yields $\dot{M} \approx 5 \times 10^{-9}\,M_\mathrm{J}\,\mathrm{yr}^{-1}$ when using scaling relationships for planetary masses, and $\dot{M} \approx 0.1 \times 10^{-9}\,M_\mathrm{J}\,\mathrm{yr}^{-1}$ with extrapolated stellar scalings. Several of these lines represent the first detections at an accretor of such low mass. The weak accretion rate implies that formation is likely over. This analysis shows that JWST can be used to measure low line-emitting mass accretion rates onto planetary-mass objects, motivates deeper searches for the mass reservoir feeding TWA 27B, and hints that other young directly imaged objects might—hitherto unbeknownst—also be accreting.

1. Introduction

While several hundreds of substellar objects display convincing evidence of ongoing accretion (Betti et al. 2023), only a few have masses below $M_\mathrm{p} \approx 10\,M_\mathrm{J}$ and have been studied extensively in the last few years: PDS 70 b and c (Wagner et al. 2018; Haffert et al. 2019) and Delorme 1(AB)b (Eriksson et al. 2020; Betti et al. 2022a, 2022b; Ringqvist et al. 2023). It is therefore capital to enlarge this population to study the dependence of the accretion rate on object mass and age, with the prospect of better understanding the differences in formation processes from stars down to planets.

Brown dwarfs and gas giants likely gain mass through different but not necessarily mutually exclusive physical mechanisms: magnetospheric accretion from a local gas reservoir (e.g., Calvet & Gullbring 1998; Hartmann et al. 2016; Thanathibodee et al. 2019; Hasegawa et al. 2024) or large-scale direct accretion onto the surface of the object and its circumplanetary disk (CPD; or "circum-substellar-object disk"; e.g., Tanigawa et al. 2012; Aoyama et al. 2018; Marleau et al. 2023). These modes of accretion are expected to produce line emission, strongest in the lines of neutral hydrogen. The mass of the accretor is a key determinant of the physical conditions at

the accretion shock on its surface or on the CPD. In turn, these conditions lead to predictions allowing one to distinguish the mechanisms. This is starting to be leveraged (Demars et al. 2023), but line-resolved ($R \gtrsim 15{,}000$) observations will be required to take advantage of the full diagnostic potential (Marleau et al. 2022).

If only an integrated line luminosity is available, as is often the case, care must be taken to use an appropriate scaling relationship to estimate the accretion rate from the line luminosity (Betti et al. 2023). Blindly extrapolating stellar relationships does not seem justified and in fact likely underestimates accretion rates systematically, by up to a few orders of magnitude (Aoyama et al. 2021; Marleau & Aoyama 2022). Nevertheless, both for spectroscopically resolved and nonresolved (low-resolution or photometric) observations, sensitivity to low line fluxes is critical to avoid being biased toward high fluxes and thus accretion rates; only nonbiased observations allow meaningful studies of the scatter in the $M(\dot{M})$ correlation and its dependence on physical parameters such as age (Betti et al. 2023).

In a wider context, the James Webb Space Telescope (JWST; Gardner et al. 2023) has a tremendous potential to help answer outstanding questions in planetary accretion and formation. The advantages of JWST are manifold. First, JWST can access bright hydrogen α-transitions, such as Paα and Brα (respectively, at 1.875 and 4.051 μm), which are challenging to observe from the ground due to Earth's atmospheric absorption. Traditionally, infrared (IR) observations have played a

crucial role as a powerful probe in star-forming regions with high extinction, which are not amenable to UV and visible observations. Second, medium-resolution spectroscopy ($R \sim 2000$) using an integral field unit (IFU) with wide wavelength coverage enables the direct detection of multiple IR emission lines in substellar companions. Near-simultaneous observations are devoid of short-term variability (e.g., GQ Lup B; Demars et al. 2023), enabling the acquisition of reliable results from the analysis of multiple lines. Lastly, JWST provides diffraction-limited observations, resulting in unprecedented sensitivity. This is a particular advantage for observing isolated substellar objects that are generally challenging to observe with ground-based adaptive optics due to their intrinsic faintness. JWST will characterize more accreting free-floating planets. For reference, the JWST sensitivity at near-IR wavelengths is approximately 100 times better than from the ground (see the "Historical Sensitivity Estimates" on the JWST website). These observations are crucial for understanding very faint lines from substellar objects in a quiescent accretion phase (e.g., Brittain et al. 2020) or with very weak accretion close to the end of their formation, which might occur earlier than thought (e.g., Wagner et al. 2023).

With its mass of $M_{\rm p} \approx 5\,M_{\rm J}$, TWA 27B, also known as 2M1207b, is the first planetary-mass directly imaged object. It was discovered by Chauvin et al. (2004), followed four years later by the iconic HR 8799 system (Marois et al. 2008, 2010). However, TWA 27B has a mass ratio of only $q \approx 0.2$ relative to the primary TWA 27A, which suggests the system might have formed not in a planetary but rather a stellar way (Lodato et al. 2005; Mohanty et al. 2013; Reggiani et al. 2016; Bowler et al. 2020).

Luhman et al. (2023) analyzed the GTO 1270 (PI: S. Birkmann) JWST/NIRSpec (Jakobsen et al. 2022) IFU (Böker et al. 2022) data on TWA 27B. Thanks to clear hydrogen-line emission, they showed that this object is accreting. They focused on the photospheric emission and measured the flux contained in one hydrogen transition, Paβ. Here, we search systematically for hydrogen lines and report the continuum-corrected line fluxes. We then use scaling relationships between line and accretion luminosity to estimate the accretion rate, and argue robustly that the line fluxes are not dominated by chromospheric activity.

2. Data and Methods

2.1. Data Sources

The JWST data were presented in Luhman et al. (2023) and were obtained with the NIRSpec instrument. They consist of 1 hr exposures starting on 2023 February 7 at 17:52:28.779 with the G395H/F290LP high-resolution-grating-filter combination (0.97–1.89 μm; after this overview, the filter names will be dropped for conciseness), at 18:32:50.598 with G235H/F170LP (1.66–3.17 μm), and at 19:11:59.463 with G140H/F100LP (2.87–5.27 μm). The spectrum for each half-grating and the error bars were kindly shared by K. Luhman. Some of the flux error bars were spuriously high, and we replaced them with the median of the well-behaved errors. In any case, the dominant source of noise is the continuum noise, as shown below.

In addition to JWST data, we provide an Hα photometric point from our analysis of Hubble Space Telescope (HST) archival data. HST observed the TWA 27 system with WFC3/

UVIS on 2011 March 28 (Program ID: 12225, PI: A. Reiners), and we show the F656N image in Appendix A. The HST image does not yield a significant detection of TWA 27B (only a tentative one) and provides an upper limit on its Hα emission. We will use this in Section 3.2.

2.2. Fitting Approach

We searched the JWST data for a signal at the metastable neutral helium triplet He I λ10833 as well as all hydrogen lines covered by the detectors in the Paschen-transition series (electron final energy level $n_f = 3$), which is $n_i = 4$–7 (Paα–Paδ); all lines up to an initial level $n_i = 10$ (Br10) in the Brackett series ($n_f = 4$); and all lines up to $n_i = 10$ (Pfϵ) in the Pfund series ($n_f = 5$), but without Pfα ($n_i = 6$) since it is off the red edge of NIRSpec, with $\lambda_0 = 7.46\,\mu$m. An overview of the lines is in Table 1. From the Humphreys series ($n_f = 6$), only the transitions $n_i = 10$–12 or 13 (5.128–4.170 or 4.376 μm, respectively; $n_i = 13$ is on the detector edge) are covered by NIRSpec, and a visual inspection did not reveal any significant peak at the respective locations. Therefore, we do not analyze this series.

In Figure 1(a), we show as an example the Paα line, covered by G140H and G235H. We show the data from each grating but also the data from G140H downgraded to the resolution of G235H. For this, we convolved the G140H data with a Gaussian of width Δv given by $\Delta v^2 = \Delta v_2^2 - \Delta v_1^2$, where Δv_1 (Δv_2) corresponds to the resolution of G140H (G235H) at Paα, $R = 3769$ ($R = 2129$), as reported in Table 1. As a reminder, the Gaussian function used for smoothing and as the line profile shape in the analysis is $X = X_0 \exp[-0.5(v/\Delta v)^2]$, where X is the filter height or the flux density and v is the Doppler velocity offset from the vacuum central wavelength. When compared at a similar resolution, the flux levels are mostly consistent in absolute value. A few features are seen in the down-resolved G140H data but not in G235H, suggesting that the error bars are still somewhat estimated. However, the overall agreement is very good.

For each line, we fitted the local continuum by a cubic function and the line excess by a Gaussian profile, using `gnuplot`'s built-in `fit` routine. We took a three-step approach:

1. We fitted the continuum in a range $\Delta v_{\rm cont} = 2700\,{\rm km\,s^{-1}}$ on either side of the theoretical vacuum line center (Wiese & Fuhr 2009), masking out $|v| \equiv \Delta v_{\rm mask} = 300\,{\rm km\,s^{-1}}$. This value of $\Delta v_{\rm cont}$ prevents the He I and Paγ lines, separated by only about 2900 km s^{-1}, from interfering with each other, and $\Delta v_{\rm mask}$ is a few times the expected line width for an $M_{\rm p} \approx 5\,M_{\rm J}$, $R_{\rm p} \approx (1$–$2)\,R_{\rm J}$ object (Luhman et al. 2023), which is conservatively at most $\Delta v \approx v_{\rm ff,\infty}$ (Aoyama et al. 2018), where $v_{\rm ff,\infty} = \sqrt{2GM_{\rm p}/R_{\rm p}} \approx 120\,{\rm km\,s^{-1}}$ is the freefall velocity from infinity. For two lines, the grating edge shortened slightly the actual wavelength range used for the continuum on the red side (Brα at $+1300\,{\rm km\,s^{-1}}$ and Paα at $+2200\,{\rm km\,s^{-1}}$), compared to the nominal $\Delta v_{\rm cont} = 2700\,{\rm km\,s^{-1}}$, but this is inconsequential. An important outcome of this fitting is the rms deviation from the fitted continuum (more properly, the *standard deviation*, but we adopt the common usage). This continuum rms is a source of noise because we do not attempt to identify and remove spectral features.
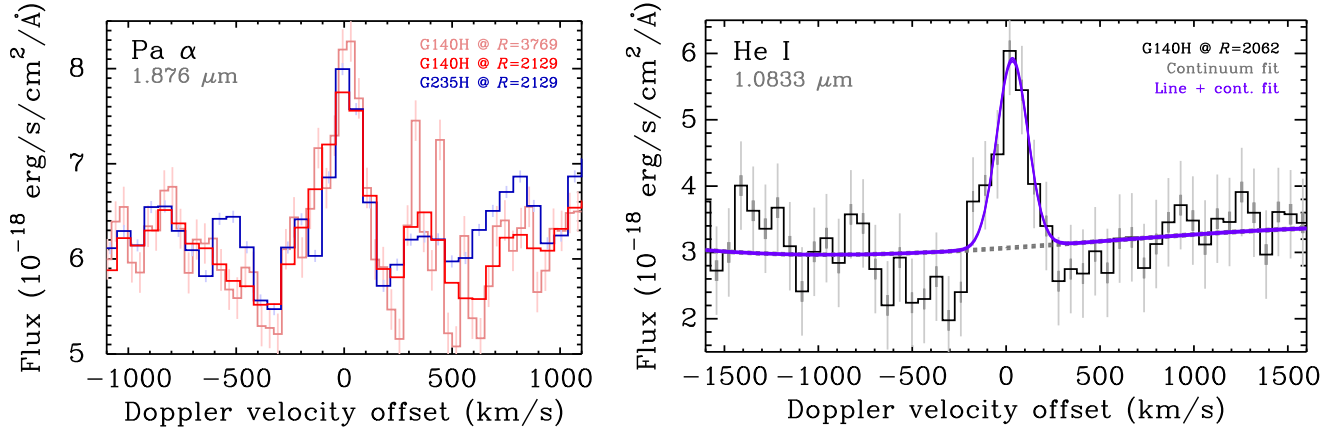
Figure 1. Left: the Paα line through the red half of the G140H (red) and the blue half of the G235H (blue) gratings at full resolution (pale red and bright blue), and from G140H down-convolved and reinterpolated to the resolution of G235H (bright red). Right: He I data (black) with error bars (pale gray, only from each bin; dark gray, adding the continuum rms in quadrature), cubic fit to the continuum (gray dashed line), and fit to the continuum and line (purple). The continuum rms noise is shown in Figure 7.

Table 1
Helium-triplet and Hydrogen Lines Covered by Luhman et al. (2023)'s JWST Spectrum of TWA 27B

Line	λ_0 (μm)	$\mathcal{F}_{\rm cont}/10^{-18}$ (erg s^{-1} cm^{-2} Å^{-1})	$F_{\rm line}/10^{-17}$ (erg s^{-1} cm^{-2})	$L_{\rm line}$ ($10^{-9} L_\odot$)	R	N_σ^F	v_0 (km s^{-1})	Δv (km s^{-1})	$\mathcal{R}_{\Delta v}$
He I$_1$	1.083	3.05 ± 0.65	2.16 ± 0.50	2.81 ± 0.65	2062	4.3	32 ± 12	84 ± 13	1.4
Paα$_1$	1.876	6.02 ± 0.61	2.41 ± 0.67	3.13 ± 0.88	3769	3.6	6 ± 12	70 ± 13	2.1
Paα$_2$	1.876	6.33 ± 0.41	1.44 ± 0.33	1.88 ± 0.43	2129	4.4	11 ± 11	50 ± 12	0.8
Paβ$_1$	1.282	5.98 ± 0.62	2.72 ± 0.61	3.54 ± 0.79	2461	4.5	17 ± 10	91 ± 11	1.8
Paγ$_1$	1.094	3.20 ± 0.50	1.57 ± 0.31	2.04 ± 0.40	2084	5.1	24 ± 9	67 ± 9	1.1
Paδ$_1$	1.005	2.12 ± 0.61	1.58 ± 0.40	2.06 ± 0.52	1908	3.9	17 ± 16	78 ± 16	1.2
Brα$_3$	4.052	3.81 ± 0.10	0.56 ± 0.24	0.73 ± 0.31	2780	2.3	47 ± 25	70 ± 26	1.5
Brβ$_2$	2.626	6.05 ± 0.23	0.73 ± 0.23	0.95 ± 0.30	3052	3.2	-16 ± 14	46 ± 14	1.1
Brγ$_2$	2.166	8.75 ± 0.22	0.50 ± 0.21	0.65 ± 0.27	2478	2.4	5 ± 22	51 ± 23	1.0
Brδ$_2$	1.945	6.69 ± 0.32	<1.32	<1.72	2213	0.7	⋯	⋯	⋯
Brε$_1$	1.818	6.80 ± 0.62	<1.47	<1.92	3629	0.2	⋯	⋯	⋯
Brε$_2$	1.818	6.55 ± 0.35	<1.48	<1.92	2061	0.4	⋯	⋯	⋯
Br10$_1$	1.737	7.90 ± 0.56	<1.36	<1.76	3438	0.5	⋯	⋯	⋯
Br10$_2$	1.737	7.85 ± 0.36	<1.52	<1.97	1965	2.2	⋯	⋯	⋯
Pfβ$_3$	4.654	2.71 ± 0.07	<0.48	<0.62	3239	1.4	⋯	⋯	⋯
Pfγ$_3$	3.740	4.80 ± 0.08	0.21 ± 0.07	0.27 ± 0.09	2549	3.0	-32 ± 17	27 ± 52	0.6
Pfδ$_3$	3.297	5.25 ± 0.10	0.35 ± 0.14	0.45 ± 0.18	2231	2.6	-35 ± 21	49 ± 24	0.9
Pfε$_2$	3.039	5.25 ± 0.20	<0.81	<1.05	3610	1.0	⋯	⋯	⋯
Pfε$_3$	3.039	5.20 ± 0.14	<0.96	<1.25	2050	2.1	⋯	⋯	⋯

Note. We consider all hydrogen lines covered by NIRSpec, but limited to an initial level $n_i \leqslant 10$ in the Brackett ($n_f = 4$) and Pfund ($n_f = 5$) series. The subscripts indicate the grating (1: G140H; 2: G235H; 3: G395H), with Paα, Brε, Br10, and Pfε covered by two gratings. $\mathcal{F}_{\rm cont}$ is the fitted continuum level at λ_0, with uncertainty $\sigma_{\mathcal{F}_{\rm cont}}$ given by the rms computed over $\Delta v_{\rm cont} = \pm 2700$ km s^{-1} (see text). $F_{\rm line}$ and $L_{\rm line}$ are the continuum-subtracted, line-integrated flux and luminosity. R is the spectral resolution at λ_0. N_σ^F is the significance of the integrated line flux or the peak significance; the peak flux density is $\mathcal{F} = \mathcal{F}_{\rm cont} + \mathcal{F}_0 = \mathcal{F}_{\rm cont} + N_\sigma^F \sigma_{\mathcal{F}_{\rm cont}}$. Δv and v_0 are the fitted Doppler line width and velocity offset of the peak. $\mathcal{R}_{\Delta v}$ is the fitted line width relative to the instrumental broadening; values below unity suggest the continuum is overestimated. For lines clearly not detected (see Section 2.3), $F_{\rm line}$ and $L_{\rm line}$ are 3σ upper limits (see text).

2. We fitted each continuum-subtracted line with a Gaussian function, again taking only the bin error bars into account.
3. We initialized the fit parameters of the continuum and line excess to the values from the sequential fits and did a joint fit. For the error bars of each bin, we added in quadrature to the error bar of each bin the rms of the continuum. The fits converged in around ≈5–20 iterations, typically around 10.

An example outcome is shown in Figure 1(b). We varied $\Delta v_{\rm cont}$ and $\Delta v_{\rm mask}$ and obtained essentially the same fit results

for all the lines (not shown). We note that the continuum rms dominates the noise budget (see the pale and dark gray error bars in Figure 1(b)).

As a comparison, we also performed the fits using only the flux uncertainty in each bin as the error bar. Some fitted lines were narrower than the instrumental broadening, but within only 1σ, and the overall results were very similar. Other variations in the approach also led, if at all, to small differences of at most a few kilometers per second in the line widths. Thus, the precise treatment of the error bars does not matter in this case.

This fitting approach yields line fluxes, always meant as an excess above the fitted continuum (see Section 3.1). The integrated luminosity of a given line is $L_{\rm line} = 4\pi d^2 F_{\rm line}$, with $d = 65.4$ pc the distance to TWA 27B (see Luhman et al. 2023 and references therein), and $F_{\rm line} = \sqrt{2\pi} \times \Delta v \times \lambda_0/c \times \mathcal{F}_0$, where Δv is the fitted Doppler-shift velocity width, $\mathcal{F}_0$ is the flux-density peak value *in excess of* the continuum, c is the speed of light, and λ_0 is the central vacuum wavelength of the transition.

For simplicity and clarity, we do not attempt to correct the fluxes for possible extinction. Interstellar extinction toward the TW Hydræ Association (TWA) and the TWA 27 system is negligible (Herczeg et al. 2004; Mohanty et al. 2007). Extinction by an edge-on disk around TWA 27B has been suggested to reconcile the tension between the spectral energy distribution-derived $T_{\rm eff}$ and theoretical predictions (e.g., Mohanty et al. 2007). However, the analysis of Luhman et al. (2023) suggests that using other atmospheric models instead might obviate the need for heavy extinction. Otherwise, somewhat "tuned" cloud properties could explain the spectrum and brightness of TWA 27B (Skemer et al. 2011). The ultimate answer is not settled, and the line-emitting regions might be differently extincted than the atmosphere. Thus, keeping the fluxes "as is" therefore avoids introducing uncertainty.

2.3. Detections and Nondetections

In this work, we qualify a line as detected only if it has more than two bins at more than 3σ. This is less stringent than the often-used 5σ criterion but appears justified given the low level of surprise, the modest impact of a detection, and the negligibility of the "Look-Elsewhere Effect," to use the considerations discussed by Lyons (2013). Unaccounted-for systematics will reduce the true significance of the detections but only modestly since the systematics seem small.

Other lines detected at 2σ–3σ will be considered only tentative detections. We report their fit parameters but do not further analyze them. Finally, for the other lines for which there is clearly no signal, we compile only upper limits on the flux and luminosity, and no fit parameters. We calculate upper limits by using an upper-tail one-sided test based on the χ^2 distribution. Specifically, we solve for the minimum line flux, which, broadened to the resolution at that wavelength, would lead to a 3σ deviation from a null excess:

$$F_{\rm line}^{\rm upp} = \frac{\Delta v_{\rm inst} \lambda_0}{c} \times \sigma_{\mathcal{F}_{\rm cont}} \times \sqrt{\frac{2\pi \chi^2_{\rm crit}}{\mathfrak{S}}} \tag{1a}$$

$$\mathfrak{S} \equiv \sum_{\rm bins} \exp^2\left[-\frac{1}{2}\left(\frac{v}{\Delta v_{\rm inst}}\right)^2\right], \tag{1b}$$

where $\Delta v_{\rm inst} = c/R/(2\sqrt{2\ln 2})$ is the effective line width given by the instrumental resolution[10] $R(\lambda_0)$, $\sigma_{\mathcal{F}_{\rm cont}}$ is the rms of the fitted continuum (i.e., its standard deviation), and $\chi^2_{\rm crit} \approx 33$ is the critical value of the χ^2 distribution that corresponds to 3σ (probability of 99.7%) for $\nu \approx 14 - 1$ degrees of freedom, since around 13–14 spectral bins are found within a (somewhat arbitrarily chosen) range of $\pm 3\Delta v_{\rm inst}$ around λ_0. We compute $\mathfrak{S}$ for each line (note the squared exponential) and always find

$\mathfrak{S} \approx 1.6$–1.7. Thus, $F_{\rm line}^{\rm upp} \approx 11.4 \times \sigma_{\mathcal{F}_{\rm cont}} \times \Delta v_{\rm inst} \lambda_0/c$. A more detailed analysis could use the injection of fake planets and take the spatially varying sensitivity into account (e.g., Bonse et al. 2023). However, since we will not analyze the nondetections in detail, we keep the simpler approach here. It is in principle more accurate than but comparable to the expression of Betti et al. (2022a), $F_{\rm line}^{\rm upp} = 3\sqrt{N_{\rm pix}} \times \sigma_{\mathcal{F}_{\rm cont}} \times \Delta\lambda_{\rm disp} = 3$–$4\,\text{Å} \times \sigma_{\mathcal{F}_{\rm cont}}$, in which $\Delta\lambda_{\rm disp} = 1.4$–$2.8\,\text{Å}\,{\rm pixel}^{-1}$ (depending on the transition) is their spectral dispersion, and $N_{\rm pix} = (7\,\text{Å})/\Delta\lambda_{\rm disp}$, or to the expression of Alcalá et al. (2014) or Gangi et al. (2022), $F_{\rm line}^{\rm upp} = 3\Delta\lambda \times \sigma_{\mathcal{F}_{\rm cont}}$, with $\Delta\lambda = 1$–$2\,\text{Å}$ as their assumed line width.

3. Results

3.1. Line Fluxes and Widths

We detect the neutral helium triplet at 4.3σ and all Paschen-series lines covered by the observations (Paα, Paβ, Paγ, Paδ) at $>3.5\sigma$–5σ. The three brightest Brackett-series lines (Brα, Brβ, Brγ) as well as Pfγ and Pfδ are tentative detections at 2σ–3σ. For the remaining hydrogen lines accessible to NIRSpec, we obtain upper limits. All detections and nondetections are presented in Table 1, and illustrated in Figure 2, with line profiles in Appendix B. One of the lines with only an upper limit is Pfϵ (on both gratings that include it), which is formally detected at 1σ–2.1σ but whose spectral appearance is clearly not credible (see last figure of Appendix B, Figure 17). All multiply detected upper limits are very similar between both detectors.

The only quantitative point of comparison with Luhman et al. (2023) concerning the line analysis[11] is the integrated Paβ line flux. They report $F_{\rm line}^{\star} = (6.6 \pm 1.2) \times 10^{-17}$ erg s^{-1} cm^{-2}, which however includes the contribution of the continuum, which we indicate with the $\star$ superscript. Our error bars are similar but only half as large. Our continuum-subtracted flux is smaller: $F_{\rm Pa\beta} = (2.7 \pm 0.6) \times 10^{-17}$ erg s^{-1} cm^{-2}. Taking the continuum to contribute simply $\Delta F = \mathcal{F}_{\rm cont} \times (\Delta v)\lambda_0/c$, where Δv is the fitted width, we obtain $F_{\rm line}^{\star} = 3.8 \times 10^{-17}$ erg s^{-1} cm^{-2}, or $F_{\rm line}^{\star} = 5.5 \times 10^{-17}$ erg s^{-1} cm^{-2} if multiplying ΔF by $\sqrt{2\pi}$ before adding it to the line excess. Thus, we agree in the recovered flux within the error bars.

We note the following points:

1. The Paα line is detected with G140H ($R \approx 3700$) and G235H ($R \approx 2100$), as shown in Figure 1(a). The integrated fluxes are almost equal, differing only by the quadratic sum of the 1σ error bars. The G235H line is nominally narrower by roughly 2σ, but this reflects the higher fitted continuum level, even though it agrees within less than 1σ with the continuum fitted on G140H. The true continuum level is unknown, and Figure 1(a) reveals that some features are absent at lower resolution, but it is unknown whether these features are real or only noise.

2. At the other lines covered by two detectors (Brϵ, Br10, Pfϵ), the respective continuum level and its uncertainty are the same to much less than 1σ between the two detectors. This suggests that the continuum is not heavily

---

[10] Obtained from the (prelaunch; dated 2016 August 30) "Dispersion curves for the NIRSpec dispersers" section of the JWST website.

[11] Apart from this, Luhman et al. (2023) showed normalized profiles only for He I, Paγ, Paβ, and Paα.
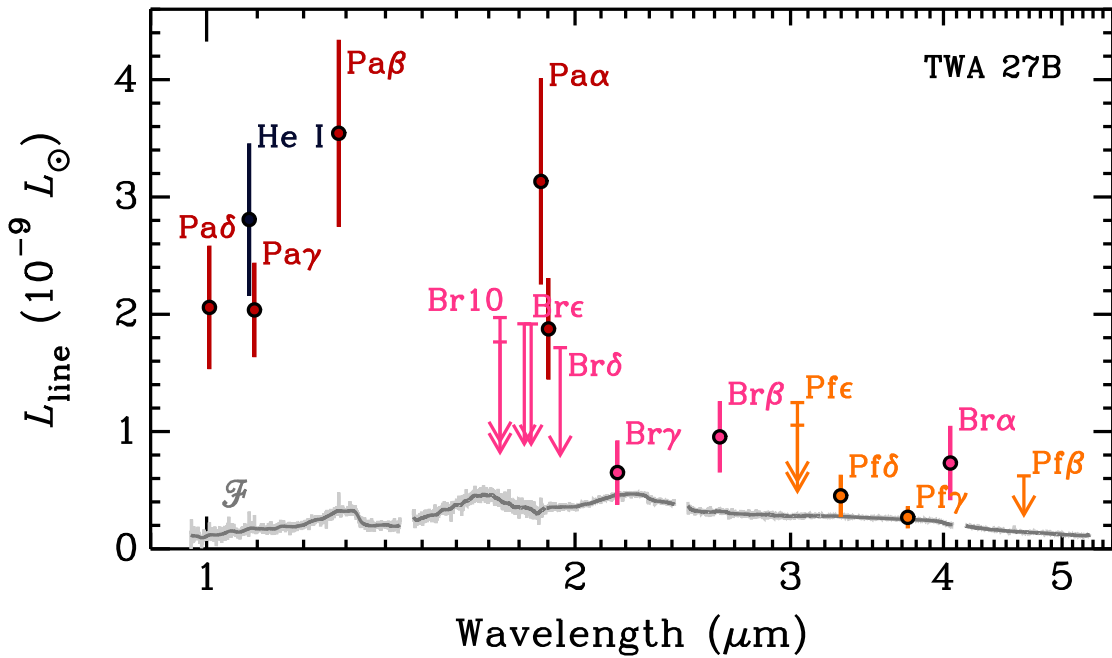
Figure 2. Summary of the line luminosities in Table 1, colored by series. Thick error bars are for clear or tentative detections, and thin arrows for 3σ upper limits (see text). $Pa\alpha_2$ and $Br\epsilon_1$ are shifted for clarity. The 3σ upper limit on $H\alpha$, $L_{\text{line}} < 6.4 \times 10^{-9}\,L_\odot$, is not shown. The spectral density $\mathcal{F}$ (at full resolution and smoothed; pale and dark gray, respectively) is shown against an arbitrary linear flux scale. The small gaps in the spectral coverage are detailed in Luhman et al. (2023).

variable on a 40 minute timescale and that there are no strong systematics between the detectors.

3. For Pfδ, a strong dip near $+2200$ km s^{-1} could lead to an overestimate of the rms and could thus reduce the significance of the line.

In Figure 3(a), we plot the line widths for the clearly detected lines (He I and the Paschen series). Paα from G235H is slightly narrower than the instrumental resolution, but by less than 1σ, which suggests that the continuum level is slightly over-estimated, and the line strength underestimated. However, all other lines (including Paα from G140H) are wider than the instrumental resolution, which means that they are somewhat resolved. In fact, assuming that both the intrinsic line shape and the instrumental point-spread function are Gaussians, we can easily estimate the intrinsic line width (that is, deconvolve) by quadratic subtraction: $\Delta v_{\text{intrsc}}^2 = (\Delta v)^2 - \Delta v_{\text{inst}}^2$. This gives $\Delta v_{\text{intrsc}} = (57 \pm 20)$ km s^{-1} for He I, 76 ± 14 for Paβ, 28 ± 22 for Paγ, 41 ± 32 for Paδ, 62 ± 15 for Paα_1 (dropping the units), where the error bars come from error propagation assuming negligible uncertainty on Δv_{inst}. Since the fitted line width is less than 1σ above the instrumental resolution at Paγ and Paδ, we will not consider them for the analysis now. The inverse-variance weighted average of the deconvolved widths is $\langle \Delta v_{\text{intrsc}} \rangle = (67 \pm 9)$ km s^{-1}. We will discuss this in Section 4. For reference, the inverse-variance weighted average of the fitted line widths is $\langle \Delta v \rangle = (73 \pm 5)$ km s^{-1}. The mean deconvolved line width is only 1.5σ smaller than this. However, $\langle \Delta v \rangle$ is in principle not a meaningful quantity because each line is instrumentally broadened by a different amount. Therefore, we will consider only Δv_{intrsc}.

The velocity zero-points v_0 (that is, the Doppler offsets from the vacuum central wavelength) are shown in Figure 3(b). The shorter-wavelength lines (He I, Paβ, Paγ, Paδ) are less consistent with zero with an average near $v_0 \approx + (20 \pm 10)$ km s^{-1}. This, and the v_0 of the Paα line from either grating, is close to or consistent with the radial velocity of the

primary of $v = + (11 \pm 2)$ km s^{-1} (Faherty et al. 2016), which is likely the systemic velocity.

3.2. Accretion Luminosity

In Figure 4, we compare the accretion luminosity L_{acc} derived from each line independently. We use the Hα upper limit (see Appendix A), $F < 1.6 \times 10^{-17}$ erg s^{-1} cm^{-2}, which we multiply by 3 to estimate the 3σ limit. We use $L_{\text{acc}}(L_{\text{line}})$ relationships of the form $\log_{10} L_{\text{acc}}/L_\odot = a \log_{10} L_{\text{line}}/L_\odot + b$, where (a, b) are fit coefficients. As in Betti et al. (2022a, 2022b), we use both the relationships for CTTSs extrapolated down to the line luminosities measured at TWA 27B, and also the $L_{\text{acc}}(L_{\text{line}})$ relationships based on detailed shock models designed for planetary-mass objects (Aoyama et al. 2021; Marleau & Aoyama 2022). We will refer to the latter as "planetary L_{acc}." Magnetospheric accretion columns could contribute to the line fluxes also for planetary-mass objects, but these models do not include this. We note that the Aoyama et al. (2018) model does not make predictions for helium lines.

Specifically, for the CTTS scalings, we use the coefficients in Alcalá et al. (2017) for all lines available, complementing with Salyk et al. (2013) for Paβ, Alcalá et al. (2014) for He I, and Komarova & Fischer (2020) for Brα. Most coefficients are summarized in Aoyama et al. (2021) and compared to the planetary values. We note that no CTTS scalings exist for Paα, Brβ, Brδ, and Pfδ.

We propagate the error from the fit and the uncertainty on the line flux. For CTTSs, the fit error is from the errors on a and b, and for the planetary relationships, we fix $\sigma = 0.3$ dex (see Aoyama et al. 2021), added through error propagation to σ from the line flux.

The inverse-variance-weighted average of the planetary L_{acc} from the detections at Paα–Paδ is $\langle \log(L_{\text{acc}}/L_\odot) \rangle = -5.23 \pm 0.14$ dex (blue dashed line and 1σ band in Figure 4). Even though the error bars are small ($\sigma \approx 0.2$ dex),
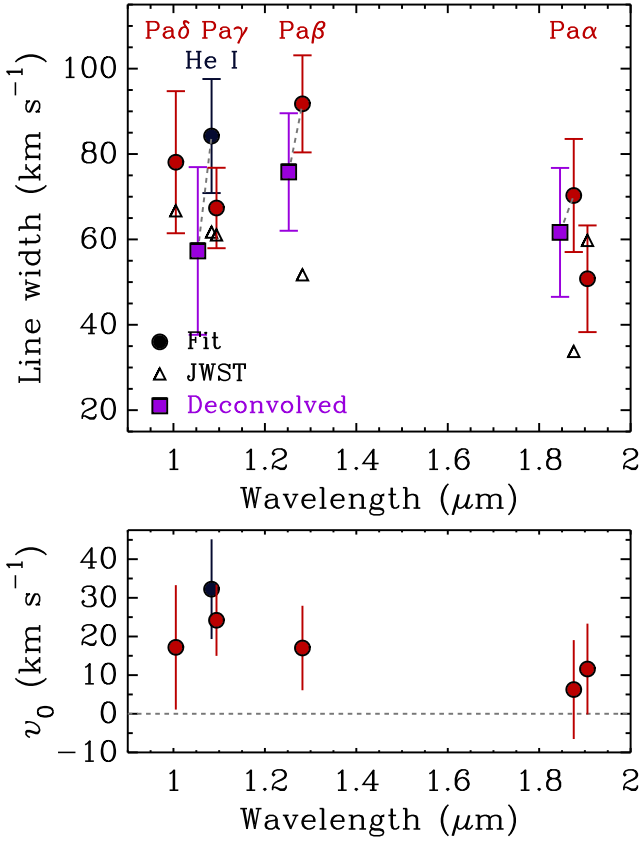
Figure 3. Analysis of the clear detections. Top: fitted line widths Δv (filled circles) and instrumental resolutions $\Delta v_{\rm inst}$ (open triangles), and deconvolved (intrinsic) line widths $\Delta v_{\rm intrsc}$ for He I, Paβ, and Paα_1 (filled squares, connected by dashed lines to Δv). They are blueshifted and Paα_2 redshifted for clarity. Bottom: line centroids.

the $L_{\rm acc}$ values from the individual lines lie within 1σ of the average. With the exception of Hα, to which we will return below, the upper limits from the other lines are consistent with this. When using the extrapolated CTTS scalings, the error bars on $L_{\rm acc}$ are larger ($\sigma \approx 0.6$ dex), but, there, too, the inferred $L_{\rm acc}$ from each line agrees within 1σ with the average $\langle \log(L_{\rm acc}/L_\odot)\rangle \approx -7$ dex (not shown). The major difference is that this is roughly 1.7 dex smaller than the average $L_{\rm acc}$ as inferred from planetary models. This is in line with the conclusions of Aoyama et al. (2021) or, for Delorme 1(AB)b, Betti et al. (2022a, 2022b).

Interestingly, the $L_{\rm acc}$ corresponding to the 3σ upper limit on $F_{\rm H\alpha}$ is lower than the average $L_{\rm acc}$ by 1 or 0.5 dex according to the planetary or CTTS relationships, respectively. This apparent discrepancy could be explained by time variability (the Hα was measured in 2011, the other lines in 2023), wavelength-dependent absorption due to dust (see Figure 9(b) of Marleau et al. 2022, but given the low accretion rate, absorption is likely negligible), or differences in the emission mechanism for Hα compared to the other lines (at least for TW Hydra, Hα does not correlate as well as the other lines with $L_{\rm acc}$; Herczeg et al. 2023). No strong arguments can be made for or against these factors. Otherwise, instrumental or other observational effects (including systematics) need to be invoked, but we assume that they cannot explain most of the 0.5–1 dex difference.

In Figure 4, we also applied the extrapolated He I $L_{\rm acc}(L_{\rm line})$ scaling relationship for CTTS, which was studied only by Alcalá et al. (2014). The helium triplet is very sensitive to both
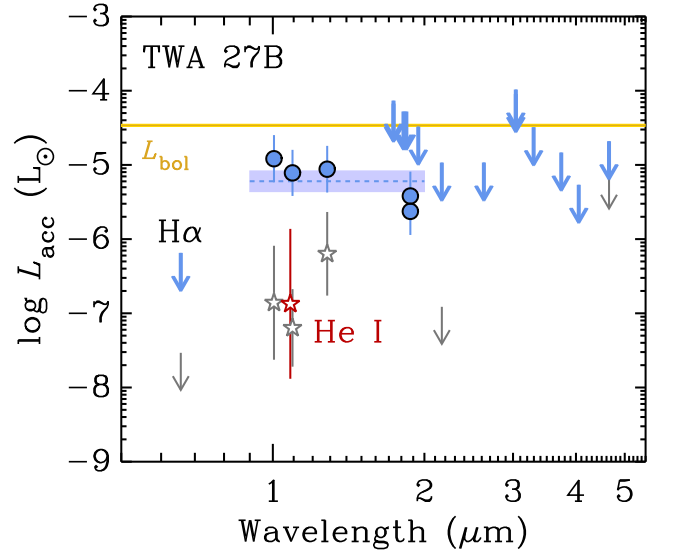
Figure 4. The accretion luminosity of TWA 27B based on scaling relationships for CTTSs (open gray stars symbols, extrapolated; Salyk et al. 2013; Alcalá et al. 2017) and for planets (filled blue circles; Aoyama et al. 2021; Marleau & Aoyama 2022). Arrows (same colors; thin and thick, respectively) show the 3σ upper limits of Table 1, with Brα for CTTSs (Komarova & Fischer 2020) outside the plot because it predicts $L_{\rm acc} \sim 10^{-10} L_\odot$. The $L_{\rm acc}$ from He I (dark red for clarity) is from Alcalá et al. (2014), without a planetary-scaling counterpart. We display the weighted mean of the $L_{\rm acc}$ inferred from planetary-shock-model scalings (blue dashed line and band). The bolometric luminosity (gold; from Luhman et al. 2023) is shown for comparison.

winds and accretion (e.g., Fischer et al. 2008; Erkal et al. 2022; Thanathibodee et al. 2022) and should be used with caution, as Alcalá et al. (2014) note. The modest resolution of the NIRSpec data, $R = 2062$, does not allow for detailed studies of the line shape (see the types proposed in Thanathibodee et al. 2022), especially since the line width is barely wider than the instrumental broadening (Figure 3(a); profile in Figure 7). Nevertheless, the $L_{\rm acc}$ inferred from He I is consistent with the average from the other lines. High-resolution line profiles could reveal whether this is a coincidence, and theoretical predictions extending the Aoyama et al. (2018) models would be welcome.

3.3. Accretion Rate

Combined with an inferred mass of $M_{\rm p} \approx 5\,M_{\rm J}$ and $R_{\rm p} = 1.4\,R_{\rm J}$ from Luhman et al. (2023), the average $L_{\rm acc}$ can be translated into an "accretion rate" $\dot{M}$, whose meaning requires discussion (see afterwards). From the planetary scalings, we obtain $\dot{M} \approx L_{\rm acc}/(GM_{\rm p}/R_{\rm p}) \approx 5 \times 10^{-9}\,M_{\rm J}\,{\rm yr}^{-1}$. Using instead the extrapolation of the Alcalá et al. (2017) CTTS relationships would imply $\dot{M} \approx 0.1 \times 10^{-9}\,M_{\rm J}\,{\rm yr}^{-1}$, while the scaling of Natta et al. (2004) applied to our $F_{\rm Pa\beta}$ value yields $\dot{M} \approx 0.3 \times 10^{-10}\,M_{\rm J}\,{\rm yr}^{-1}$. This is slightly lower than the $\dot{M} \sim 10^{-10}$–$10^{-9}\,M_{\rm J}\,{\rm yr}^{-1}$ that Luhman et al. (2023) report using that relationship. The reason is that these scalings are defined for continuum-subtracted (i.e., photospheric-emission-corrected) values, while Luhman et al. (2023) took the total line flux, leading to an overestimate by around 0.4 dex. This is comparable to the scatter in these relationships and clearly smaller than their systematic uncertainties (Betti et al. 2023), and thus not a major issue. The targets analyzed in Alcalá et al. (2017) have Paβ luminosities $L_{\rm line} \sim 10^{-6.5}$–$10^{-3}\,L_\odot$. Thus, applying this relationship to TWA 27B requires an extrapolation by 2 dex. This is only

slightly smaller than the range of data and therefore possibly acceptable, but it would require some validation.

This accretion rate, whether using the planetary scalings or the extrapolated CTTS ones, is only an estimate due to uncertainties in the prefactors (for instance due to a finite starting radius for the infall). However, even the presumably more realistic, and much higher, value from the planetary scalings implies an "accretion rate" that is small in the sense that the nominal mass doubling time $\tau = M_p/\dot{M} \sim 1$ Gyr, which is orders of magnitude longer than the age of the system (10 ± 2 Myr; Luhman 2023) or of the TWA. Thus, TWA 27B would be at the very end of its formation. This is in line with the finding that L_{acc} is smaller than the bolometric luminosity (see Figure 4) by about 0.4 dex according to planetary scalings, and even more if extrapolating the CTTS scalings. While of interest for observers and theoreticians alike, the accretion processes seem to be currently of very subdominant existential relevance for TWA 27B.

However, as discussed in Marleau et al. (2023), this $\dot{M}$ is not necessarily the growth rate of the planet but rather only what is hitting the planetary surface and/or the CPD close to the planet: in practice, gas needs to shock at $v \gtrsim 30$ km s^{-1} to emit lines[12] (Aoyama et al. 2018). TWA 27B might also be accreting through a boundary layer, which likely does not generate lines. Then, the total accretion rate would be larger than inferred. Given the mass ratio with TWA 27A ($q \approx 0.2$) and their separation (55 au), it is unclear whether physical scales comparable to or larger than the Hill sphere $R_{Hill} \approx 22$ au are feeding TWA 27B, or whether it can draw the matter it is accreting only from a CPD. There is no clear published IR flux excess (while, as Luhman et al. 2023 note, there might be in unpublished 5–28 μm MIRI data), and the Atacama Large Millimeter/submillimeter Array (ALMA) upper limit from Ricci et al. (2017) constrains little the amount of mass available in the system or the size of the mass reservoir. On the other hand, if TWA 27B is undergoing magnetospheric accretion and the columns contribute to the line emission (Hartmann et al. 2016), the line flux may indeed be tracing (nearly) the whole mass flow.

We keep these caveats in mind but compare in Figure 5 this accretion rate with those of the other TWA members. The $\dot{M}$ values are from Venuti et al. (2019), with TWA 30B excluded because it is likely severely affected by extinction (Looper et al. 2010; Rodriguez et al. 2015). In particular, toward higher-mass objects, the line luminosities might trace the entire mass flow, whereas, for the lower-mass objects (TWA 27A and TWA 28, since no lines were detected at TWA 40), the reported $\dot{M}$ values might be lower limits.

Intriguingly, the accretion rate onto TWA 27B according to the planetary scaling relationship is somewhat smaller than the CTTS-scalings-based $\dot{M}$ for TWA 27A, with an instantaneous ratio $\eta_{inst} \equiv \dot{M}_B/(\dot{M}_A + \dot{M}_B) \approx 0.2$, where $\dot{M}_A \approx 10^{-7.8} M_J$ yr^{-1} (Venuti et al. 2019). At a mass ratio $q \approx 0.2$, different hydrodynamics simulations predict on average a steady-state $\eta \approx 0.6$–0.9 (Bate 2000; Lai & Muñoz 2023). That the theoretical and observational η are only within a factor of a few from each other suggests that the $\dot{M}$ estimate using the planetary paradigm for TWA 27B might be relatively accurate. However, the
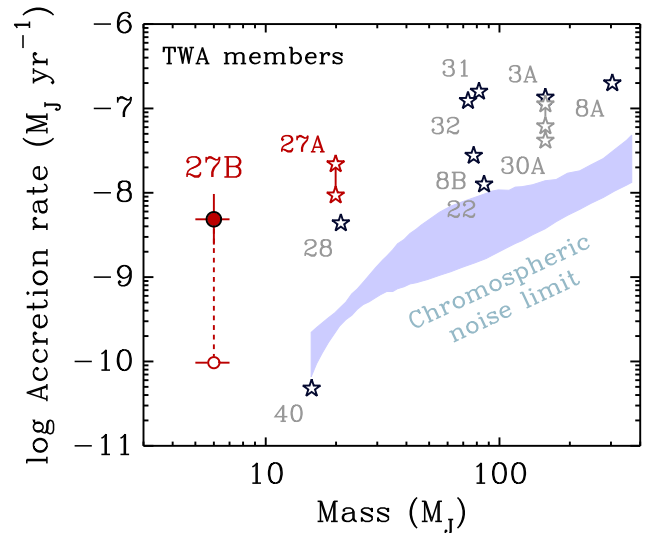
---
[12] This applies to molecular hydrogen, since it first needs to dissociate, using up energy that could otherwise go into line emission. Atomic hydrogen could emit for lower shock velocities, but at low shock velocities, the accreting hydrogen is expected to be coming in molecular form (see Figure 12(b) of Aoyama et al. 2020).

Figure 5. Accretion rates of TWA objects. We show the data of Venuti et al. (2019; gray stars; multiple observations are joined by a line; only TWA 1 is off the plot with $M \approx 600 M_J$) and add our analysis of TWA 27B using the Aoyama et al. (2021) relationships (filled circle) or the extrapolated CTTS relationships (open circle). Labels give the TWA numbers. The blue band indicates the chromospheric noise limit at 3–10 Myr from Venuti et al. (2019).

measurements are not contemporaneous (TWA 27A: taken in 2010 and 2012; TWA 27B: 2023), while accretion-rate variability is expected in binary systems on several timescales (e.g., Muñoz et al. 2020). This comparison should therefore be repeated after further monitoring.

4. Discussion

We briefly discuss some aspects of our results.

Line width. We found an average deconvolved (intrinsic) line width $\Delta v_{intrsc} = (67 \pm 9)$ km s^{-1} based on the well-resolved lines He I, Paα, and Paβ. The other clearly detected lines, Paγ and Paδ, have a fitted width barely wider than the instrumental resolution. Shock models predict the intrinsic line width to be not directly equal to but of the order of the preshock velocity (Aoyama et al. 2018; Aoyama & Ikoma 2019). The exact line width depends on the preshock conditions because they set where (at what depth and thus temperature) in the postshock region a particular line is formed. Hydrogen and helium lines might originate from different depths given the different excitation energies of the starting levels. Nevertheless, all intrinsic line widths and the average are consistent with each other to within 1σ.

If $M_p = 5 M_J$, and $R_p = 1.4 R_J$ (Luhman et al. 2023), the surface freefall velocity is $v_{ff,\infty} = 117$ km s^{-1}, so that $\Delta v_{intrsc} \approx 0.6 v_{ff,\infty}$. Qualitatively, this therefore seems to be in line with shock-model predictions. This also agrees with simulations of accretion onto gap-opening planets, which show that, while most gas falling from Hill-sphere scales lands on the CPD and not on the planetary surface (Tanigawa et al. 2012), the contribution from the planetary surface should dominate (Marleau et al. 2023). At the same time, this line width also seems broadly consistent with predictions from magnetospheric accretion (Thanathibodee et al. 2019). Thus, only a medium-resolution line profile is not sufficient to distinguish the two scenarios, and both higher-resolution observations and quantitative modeling are required (Demars et al. 2023). However, this Δv_{intrsc} matches well with the interpretation that TWA 27B

is not a higher-mass (substellar) object with an inclined disk leading to high extinction (see Luhman et al. 2007) since the higher mass would likely lead to a wider line than observed.

Chromospheric activity? Accretion at low-mass objects is a barely charted territory, and a valid concern is whether the observed line emission comes from accretion or chromospheric activity. Figure 5 shows that the $\dot{M}$ of TWA 27B is 1.5 dex above the chromospheric noise limit (Manara et al. 2013, 2017; Venuti et al. 2019) at $M_p = 20\,M_J$. How the limit behaves at lower masses, that is, closer to TWA 27B's $M_p \approx 5\,M_J$, is an open question; it might extrapolate as a power law or drop precipitously below a certain mass. However, a sharp rise by several orders of magnitude seems unlikely. Therefore, despite the statistical uncertainties in $\dot{M}$, accretion appears to be the likeliest source of the lines at TWA 27B. A similar argument can be made for Delorme 1(AB)b (Eriksson et al. 2020; Betti et al. 2022a, 2022b; Ringqvist et al. 2023).

Helium line emission. With its clear He I $\lambda10833$ emission (Luhman et al. 2023), TWA 27B joins the select club of known accretors below $\approx 20\,M_J$ exhibiting He I lines. To the best of our knowledge, the other members are Delorme 1(AB)b ($M_p \approx 12\,M_J$; detections at $\lambda\lambda6678$, 7065, 7281, 10833; Eriksson et al. 2020; Betti et al. 2022a) and 2MASS J11151597+1937266[13] ($M_p \approx 7$–$21\,M_J$; detections at $\lambda\lambda4471$, 5876, 6678, 7065; Theissen et al. 2017, 2018), with the next least massive objects around $M_p \approx 20\,M_J$ (Mohanty et al. 2005; Herczeg et al. 2009). As noted in Section 3.2, interpreting the He I line shape at stellar accretors is difficult (Kwan et al. 2007; Erkal et al. 2022), and the situation for planetary-mass accretors is unknown. Higher-resolution observations should allow disentangling possible contributions from a CPD wind, accretion funnels, or postshock emission.

5. Summary and Conclusion

We have reanalyzed the processed JWST/NIRSpec spectrum of TWA 27B presented in Luhman et al. (2023), focusing on the accretion indicators because they stated detections of three or four Paschen lines and of the He I triplet. We searched systematically for all accessible hydrogen lines, fitted and subtracted the continuum, and measured line shapes and total fluxes. We quantified the uncertainty on the line shape and integrated the flux by measuring the "photospheric noise," which is the continuum residual from the (not-modeled) atmosphere. Our results are as follows:

1. He I is detected at $>4\sigma$ and the Paschen-series lines that NIRSpec covers (Paα–Paδ) at 3.5σ–5σ. These are robust detections. The Brα, Brβ, and Brγ lines are tentatively detected with 2σ–3σ. The Pfγ and Pfδ signals are marginal. For the other lines (Brδ–Br10, Pfβ, and Pfϵ), we obtain upper limits.

2. The Paα line is covered by two grating-and-filter combinations, which observed TWA 27B ~ 40 minutes apart. The similarity of the continuum and the line shape between both observations suggests little continuum variability and no strong systematics between the gratings.

3. We independently fit each line and find that for the lines clearly detected at $>3\sigma$, namely He I, Paα_1, and Paβ, the fitted widths are well above the instrumental resolution (especially the latter two thanks to $R \approx 3800$ and ≈ 2500, respectively). Their deconvolved (intrinsic) widths are consistent with each other and averaging to $\Delta v_{\mathrm{intrsc}} = (67 \pm 9)\,\mathrm{km\,s^{-1}}$. This is around 60% of the freefall velocity at the surface of TWA 27B. The width is qualitatively consistent with shock-model predictions (Aoyama et al. 2018) and the result that the planetary-surface shock and not the CPD-surface shock should dominate the emission (Marleau et al. 2023), but also with expectations from magnetospheric accretion (Thanathibodee et al. 2019). Detailed modeling is required to relate preshock velocities and line widths and to help determine where and how the emission lines are formed.

4. We find a Paβ line-excess flux $F_{\mathrm{Pa}\beta} = (2.7 \pm 0.6) \times 10^{-17}\,\mathrm{erg\,s^{-1}\,cm^{-2}}$. Adding the contribution from the continuum, we recover to 1σ the total line flux reported by Luhman et al. (2023), $(6.6 \pm 1.2) \times 10^{-17}\,\mathrm{erg\,s^{-1}\,cm^{-2}}$, which includes the continuum.

5. Using scalings derived for CTTS (e.g., Alcalá et al. 2017) extrapolated to planetary luminosities or scalings based on detailed models yields accretion luminosities that are consistent between the different lines but discrepant by 1.7 dex between the two approaches, as found before (Betti et al. 2022a, 2022b). Correspondingly, the line-producing (shock) gas mass flow rate $\dot{M} \approx 5 \times 10^{-9}\,M_J\,\mathrm{yr^{-1}}$ is about 50 times higher according to planetary scalings than with the extrapolated CTTS relationships. If $\dot{M}$ is the growth rate of TWA 27B, its formation is over. The possibility of magnetospheric accretion and other considerations introduce uncertainties about the meaning of $\dot{M}$.

6. All integrated line luminosities are on the order of $L_{\mathrm{line}} \sim 10^{-9}\,L_\odot$. Despite theoretical uncertainties, the lines detected come robustly from accretion processes and not from chromospheric activity.

A detailed study of the atmospheric properties could help identify atomic and molecular features in the spectrum of TWA 27B. Removing them would reduce the continuum noise, improve the accuracy of the inferred line shape and flux, and increase the statistical significance by decreasing the noise. Thus, the significance of our detections might be currently underestimated. Deeper and spatially better resolved ALMA observations would be very valuable to constrain the amount of mass available in the TWA 27 system and the location of the gas reservoir from which TWA 27B is drawing.

Twenty years after its discovery, TWA 27B still holds many surprises. It could well be that also other young directly imaged companions are accreting even though no CPD has been detected so far and even if the parent disk is long gone. A deep look with JWST could be worthwhile, and our results suggest that He I, Paβ, and Paα might be particularly well-suited tracers.

---

[13] While Theissen et al. (2018) qualified the hydrogen-line emission as coming from persistent magnetic activity or weak accretion, they were assuming a distance $d = (37 \pm 6)$ pc. The updated $d = (45 \pm 2)$ pc (Gaia Collaboration et al. 2021) might imply that accretion is stronger than initially thought, and the mass somewhat higher, but this needs a quantitative reassessment.

Figures 1–5 were produced using GDL,[14] an actively developed open-source drop-in alternative to IDL. Figure 6 was made with https://github.com/AstroJacobLi/smplotlib (Jiaxuan 2023), a package that (finally!) makes the good ol' Hershey fonts SuperMongo and IDL easily available in python. Figures in Appendix B used gnuplot with the terminal pdfcairo and the font Priori Sans.

Appendix A
HST Data at Hα

In Figure 6, we show the primary-subtracted F656N image (that is, at Hα) of the TWA 27 system taken by the HST with WFC3/UVIS2. TWA 27 was observed on 2011 March 28 (Program ID: 12225, PI: A. Reiners), with an integration time of 120 s. The location of TWA 27B is indicated by a red box. The flux at the position of TWA 27B, measured in an $r = 2.5$ pixel aperture, is 2.2σ above the background, which was calculated as the standard deviation from $r = 2.5$ pixel apertures at the same angular separation as TWA 27B. Therefore, the small excess is tantalizing, but a confident Hα detection ($>3\sigma$) would require additional observations. We use the flux upper limit in Section 3.2.
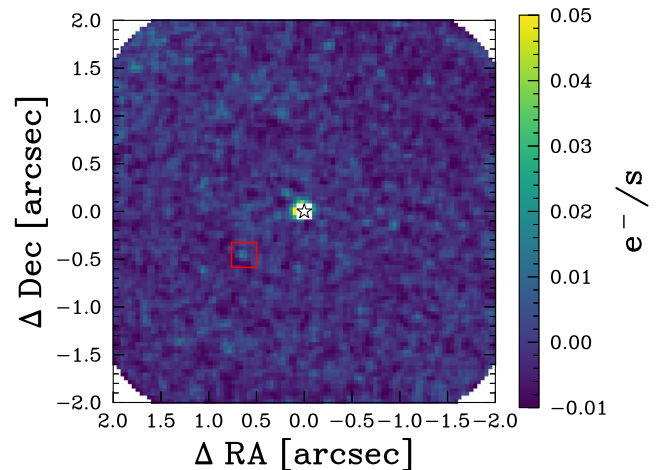
Figure 6. HST Hα (WFC3/UVIS2/F656N; $\Delta\lambda = 18$ Å, $R = 372$, $\Delta v = c/R = 807$ km s^{-1}) view of the TWA 27 system, with subtracted primary (star symbol) and nondetected companion (red box).

Appendix B
All Line Profiles

In Figures 7–17, we show profiles of the He I and the hydrogen lines for which we searched. In each case, we show a broader region with the fitted continuum (top panel) and the continuum-subtracted profile in a zoomed-in region (bottom). The integrated significance of each line, using N_σ^F from Table 1, is indicated in red below each top panel curve.
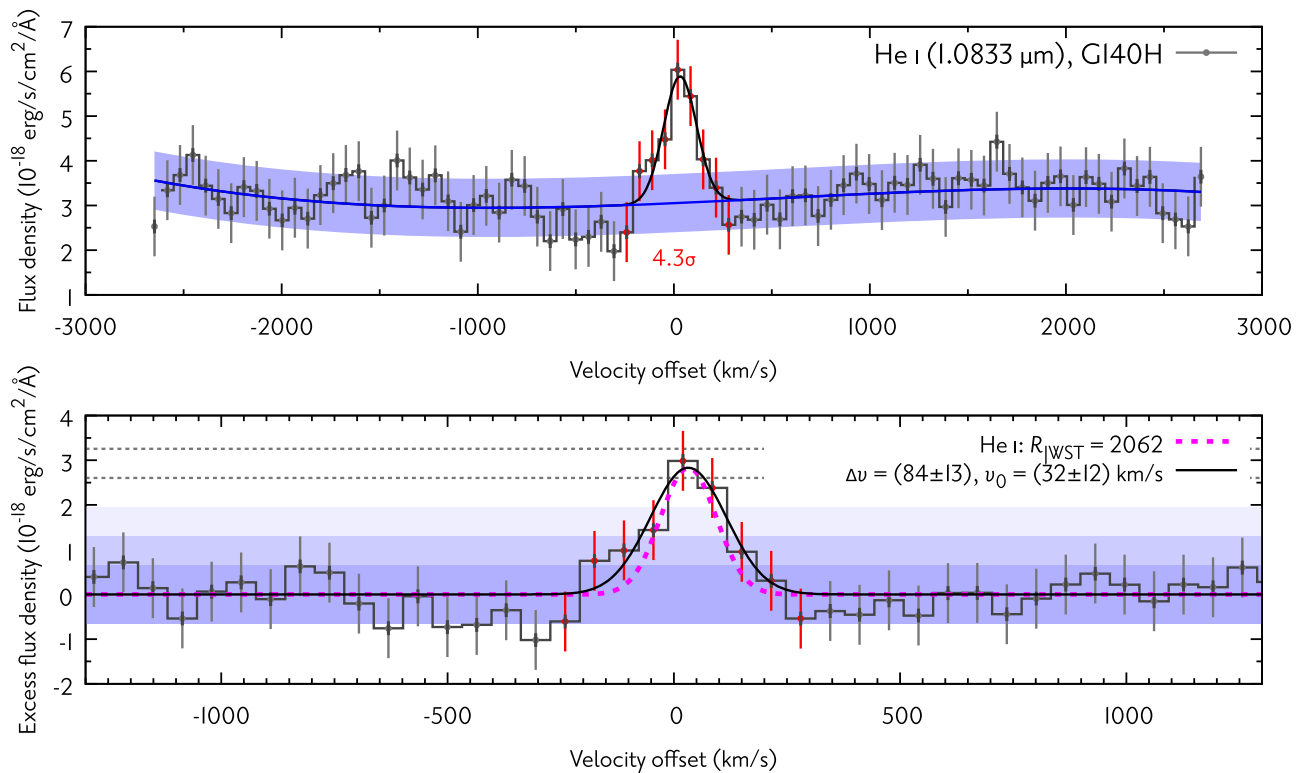
Figure 7. Line profile for He I. We show the fitted continuum and line (black) and just the continuum (blue line). Top: whole range used for calculating the continuum, excluding the points in red (close to the line center). Blue band: $\pm 1\sigma$ range (rms of continuum). Bottom: zoom-in on the continuum-subtracted line. Bands: 1σ, 2σ, 3σ. Dotted gray lines: 4σ, 5σ. Pink: instrumental broadening. The dark gray part of the error bars: only the error on the bin (as we redetermined it). Full error bar: adding the continuum rms in quadrature.
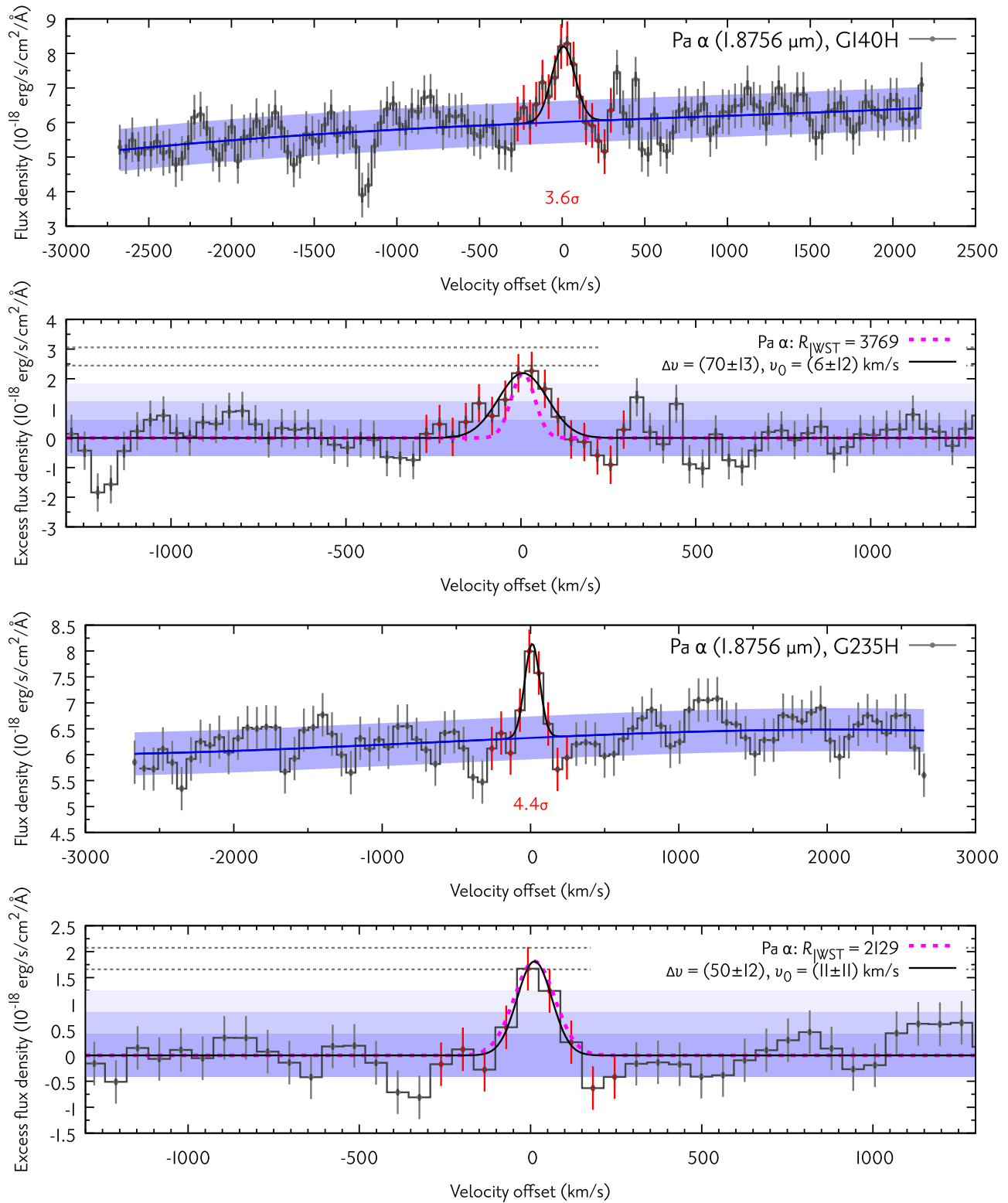
Figure 8. As in Figure 7 but for Paα on the two gratings: red half of G140H (top), blue half of G235H (bottom).
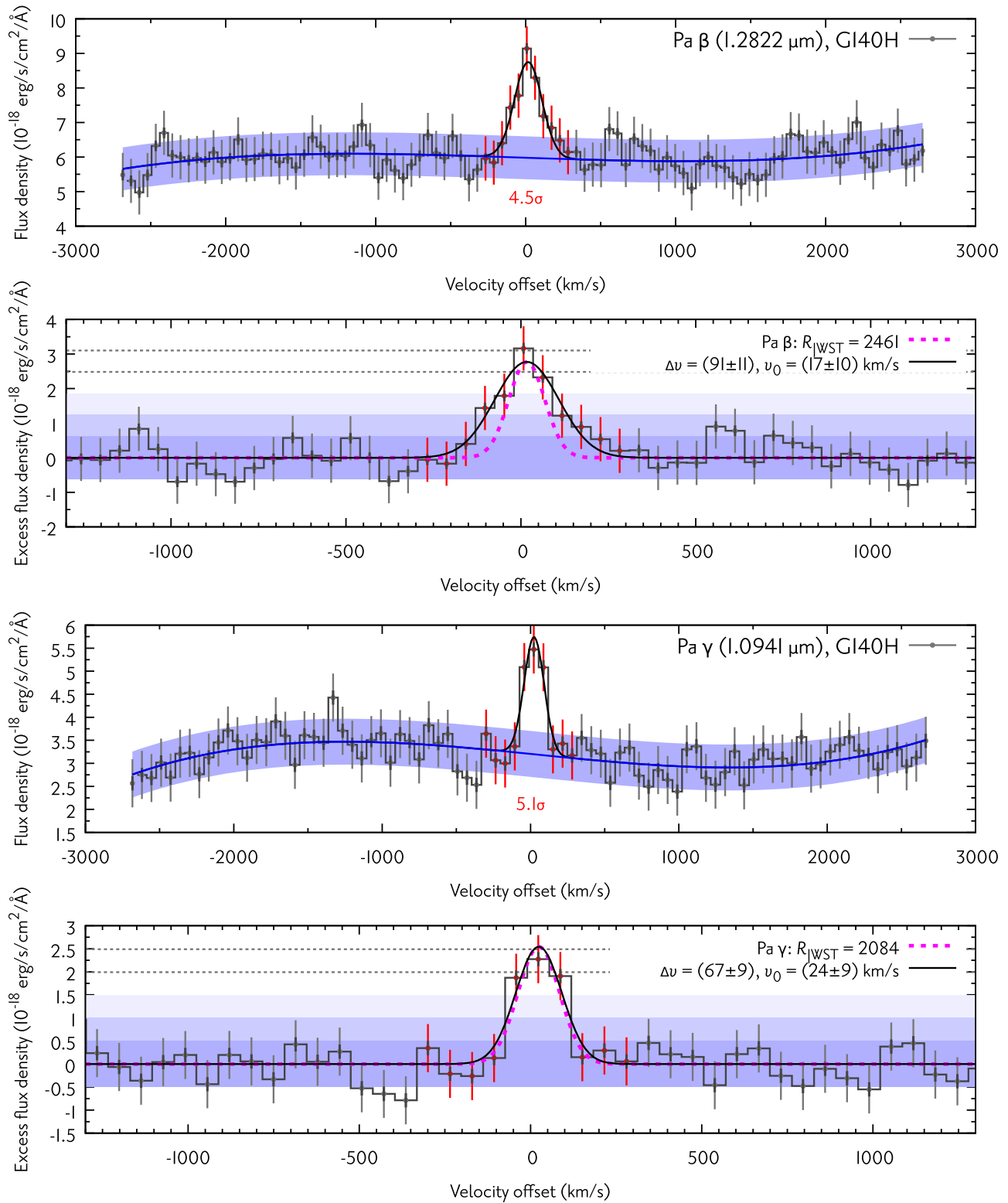
Figure 9. As in Figure 7 but for Paβ and Paγ.
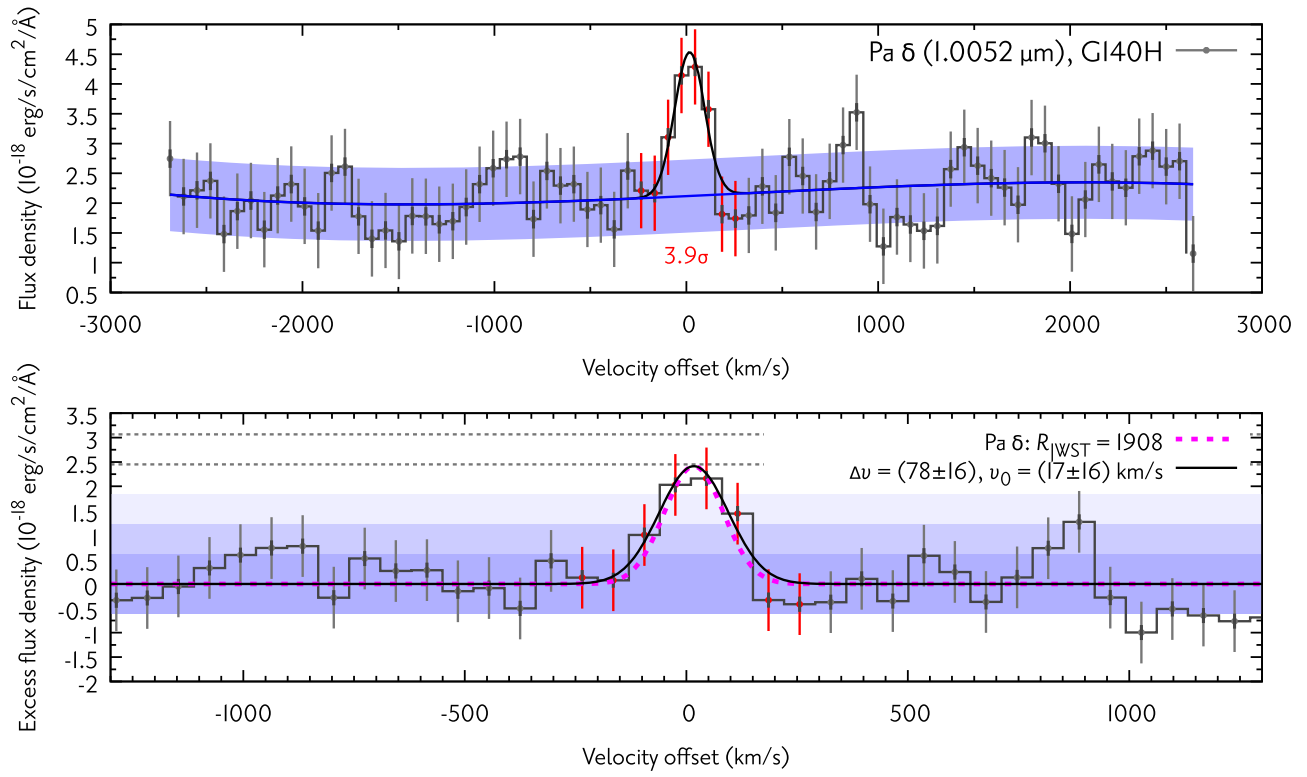
Figure 10. As in Figure 7 but for Paδ, the highest-order potentially detectable Paschen line.
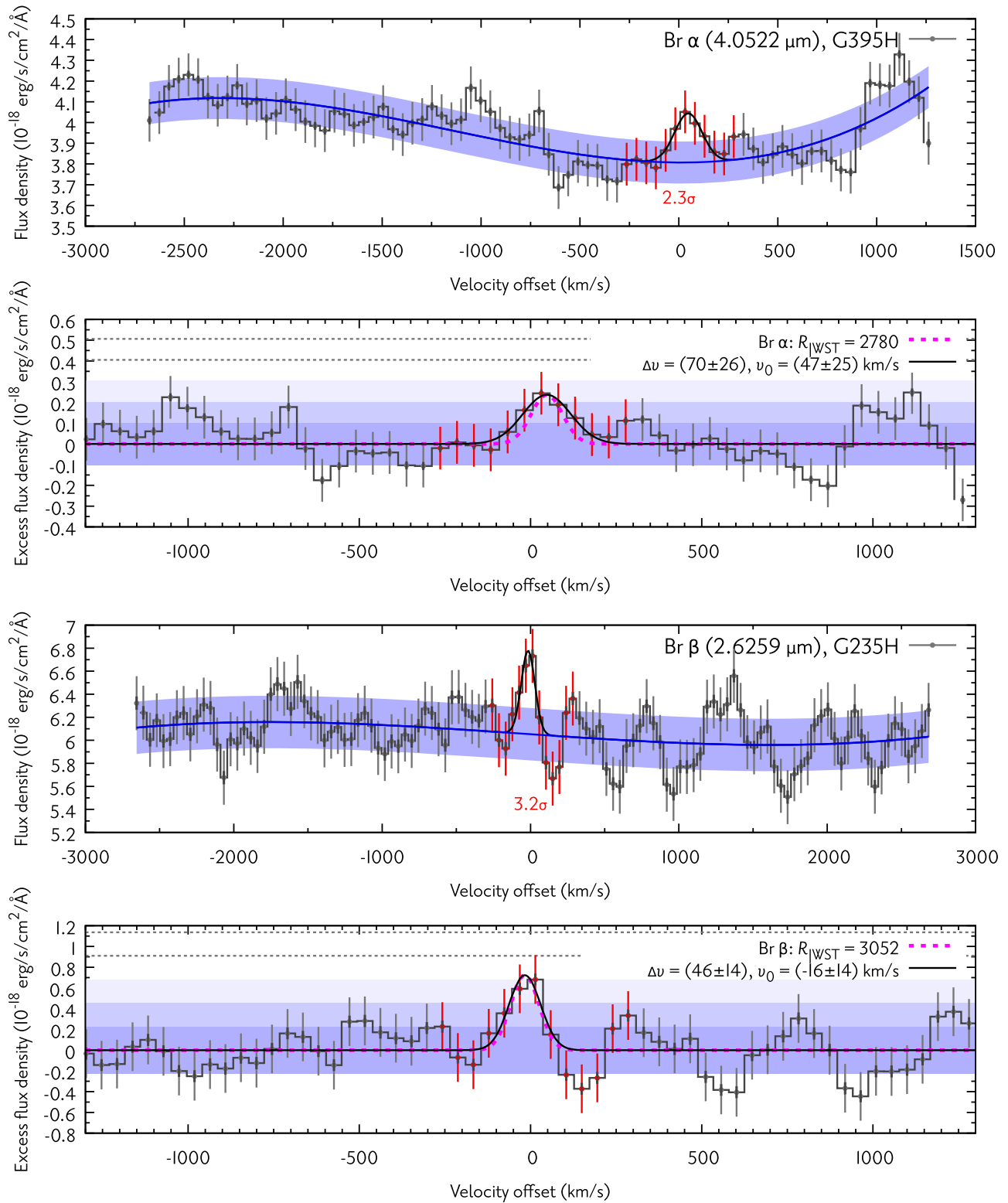
Figure 11. As in Figure 7 but for Brα and Brβ.
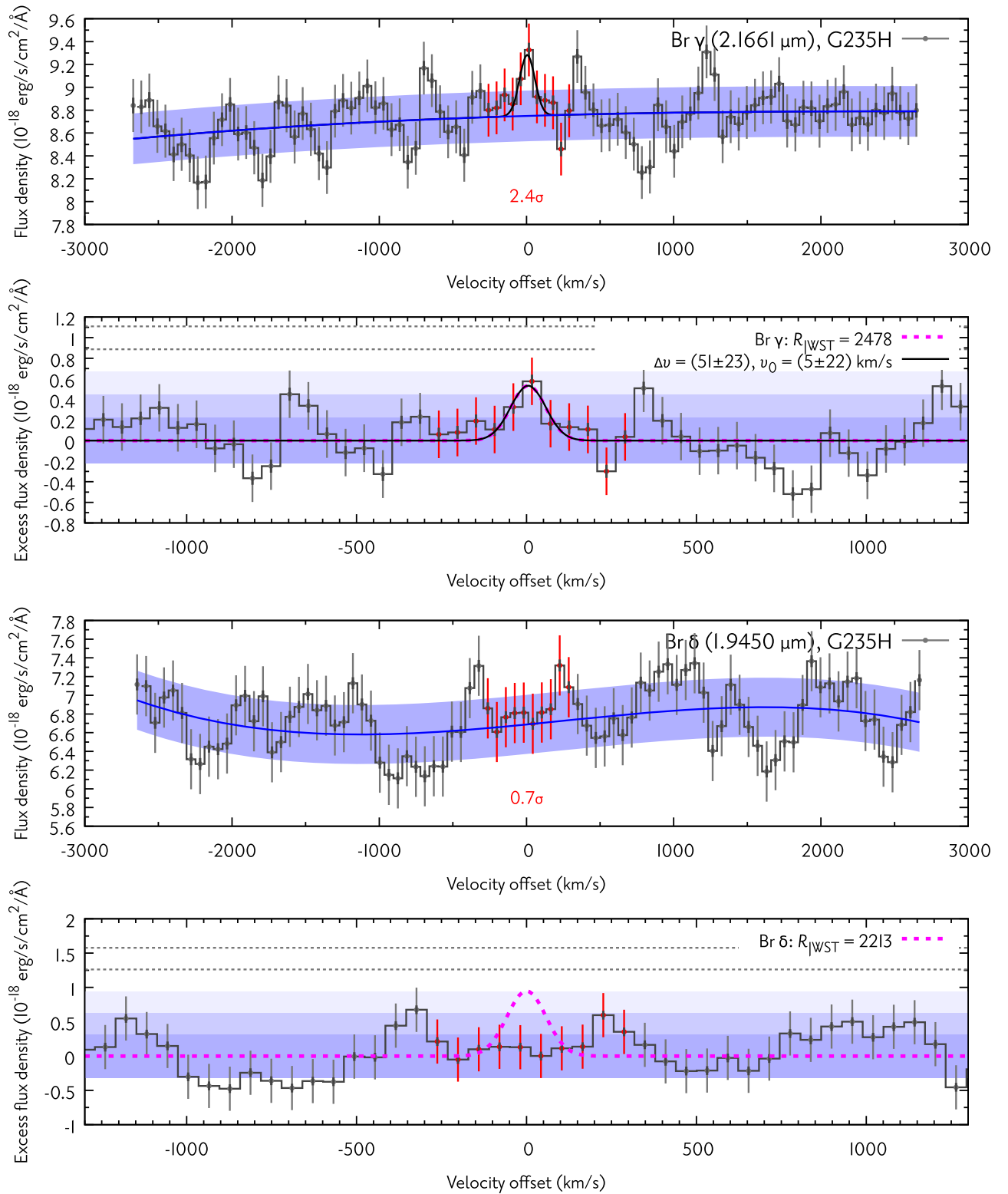
Figure 12. As in Figure 11 but for Brγ, which is tentatively detected, and for Brδ, which is a clear nondetection. For nondetections, the height of the instrumental Gaussian is set to 3σ for illustration purposes.
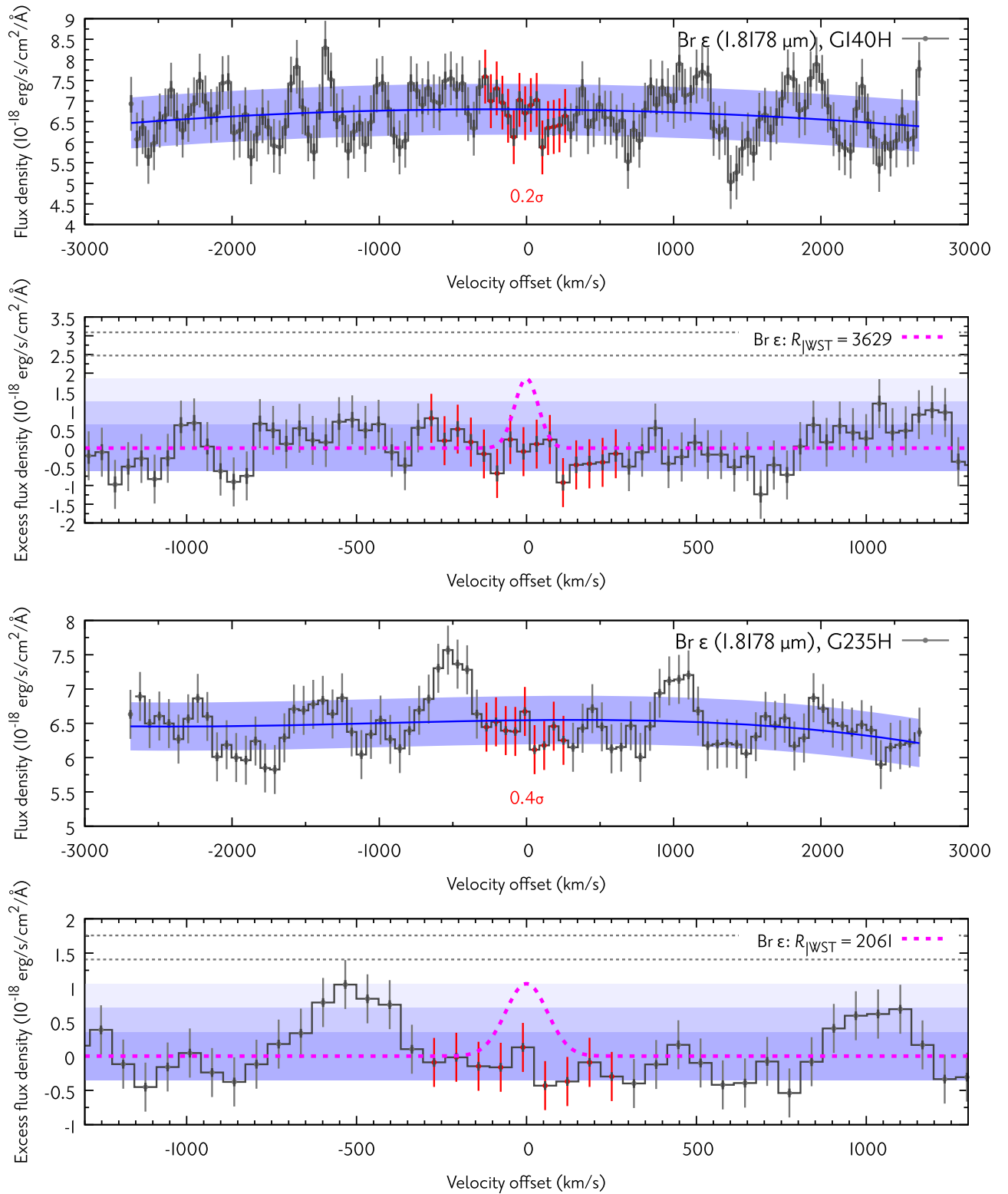
Figure 13. As in Figure 11 but for Brε (clearly nondetected) through two gratings (top: G140H; bottom: G235H).
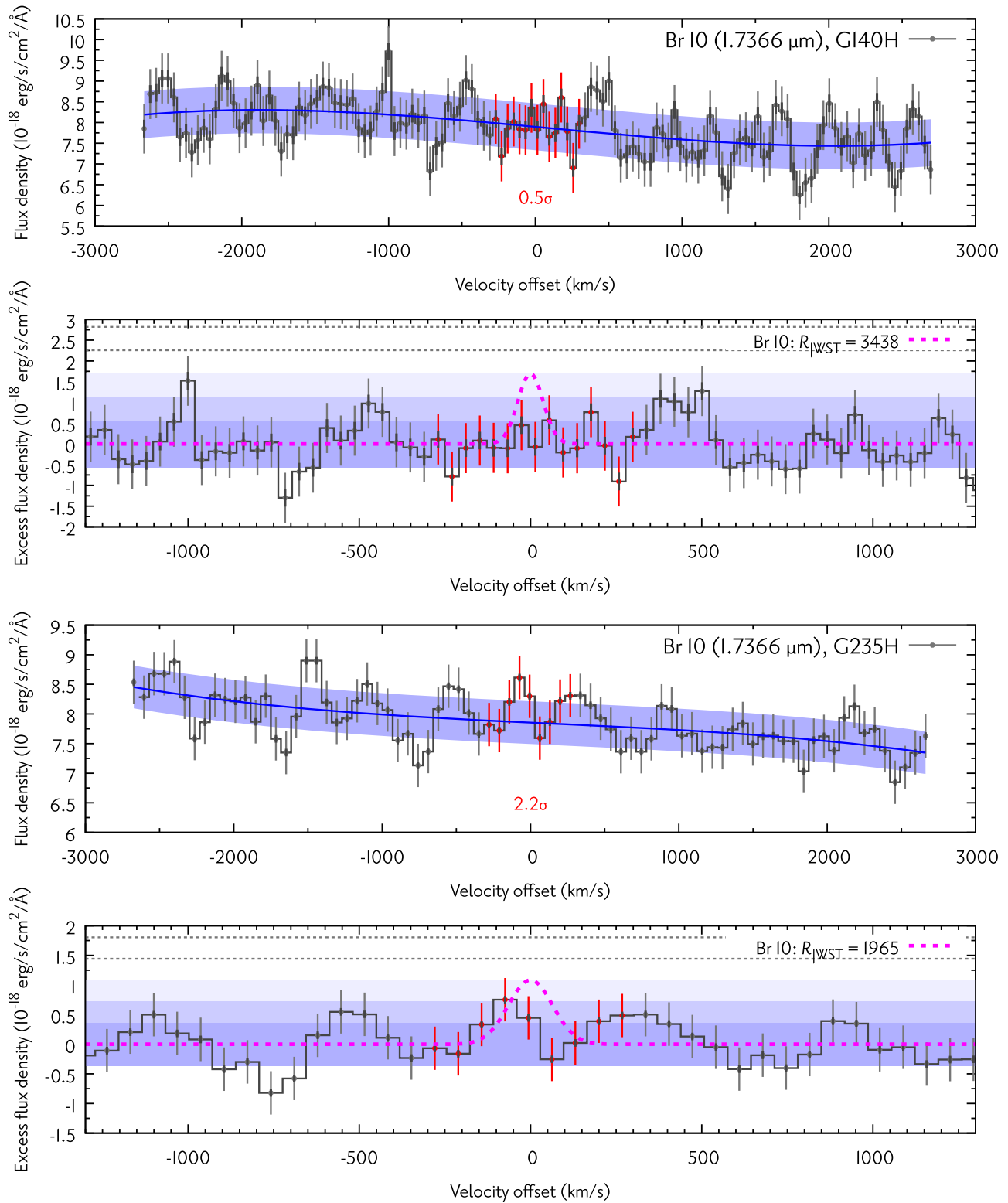
Figure 14. As in Figure 13 but for Br10 (clearly nondetected) through two gratings (top: G140H; bottom: G235H).
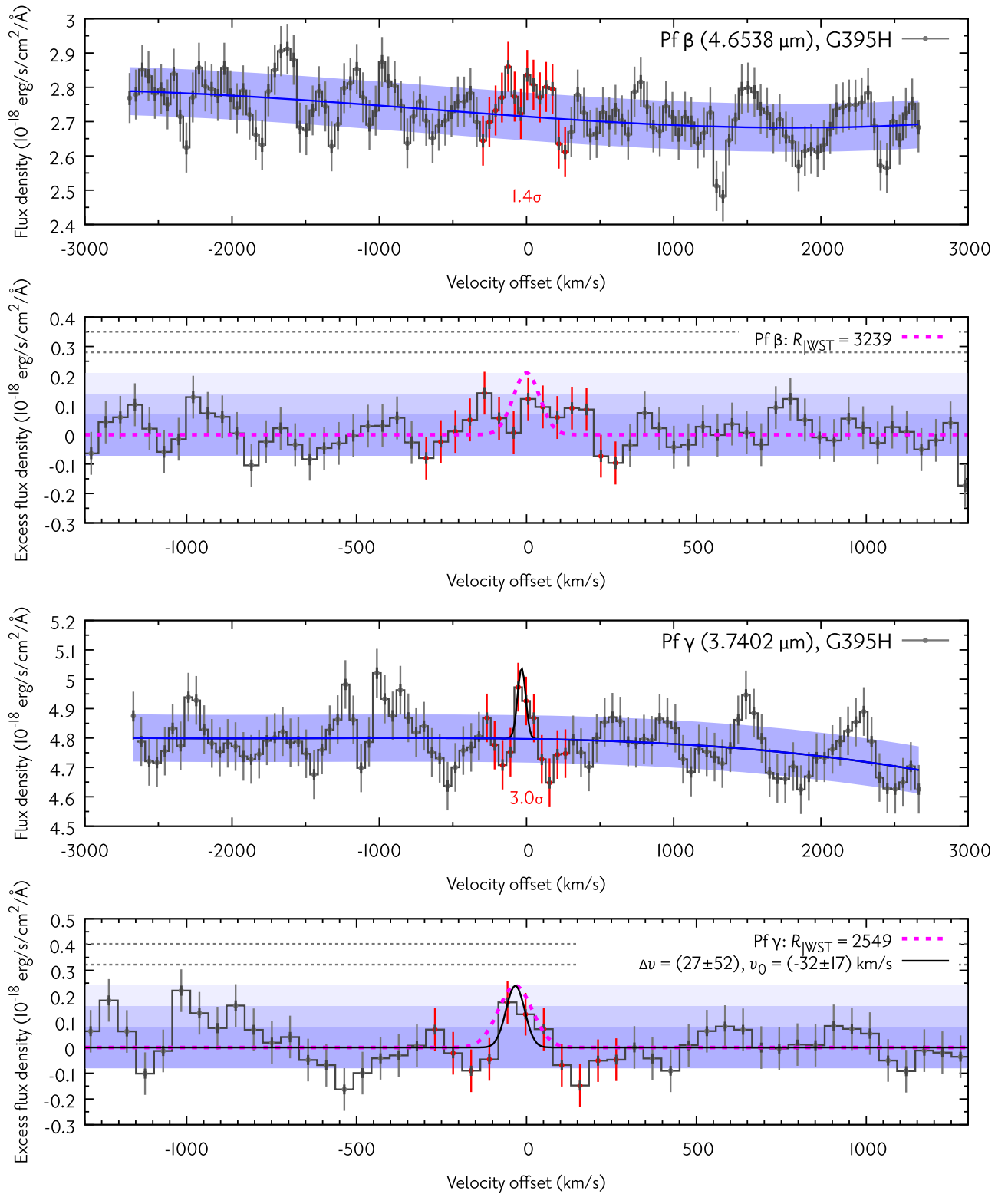
Figure 15. As in Figure 11 but for Pfβ (not detected) and Pfγ (tentatively detected, but with more significance if the continuum is in fact lower).
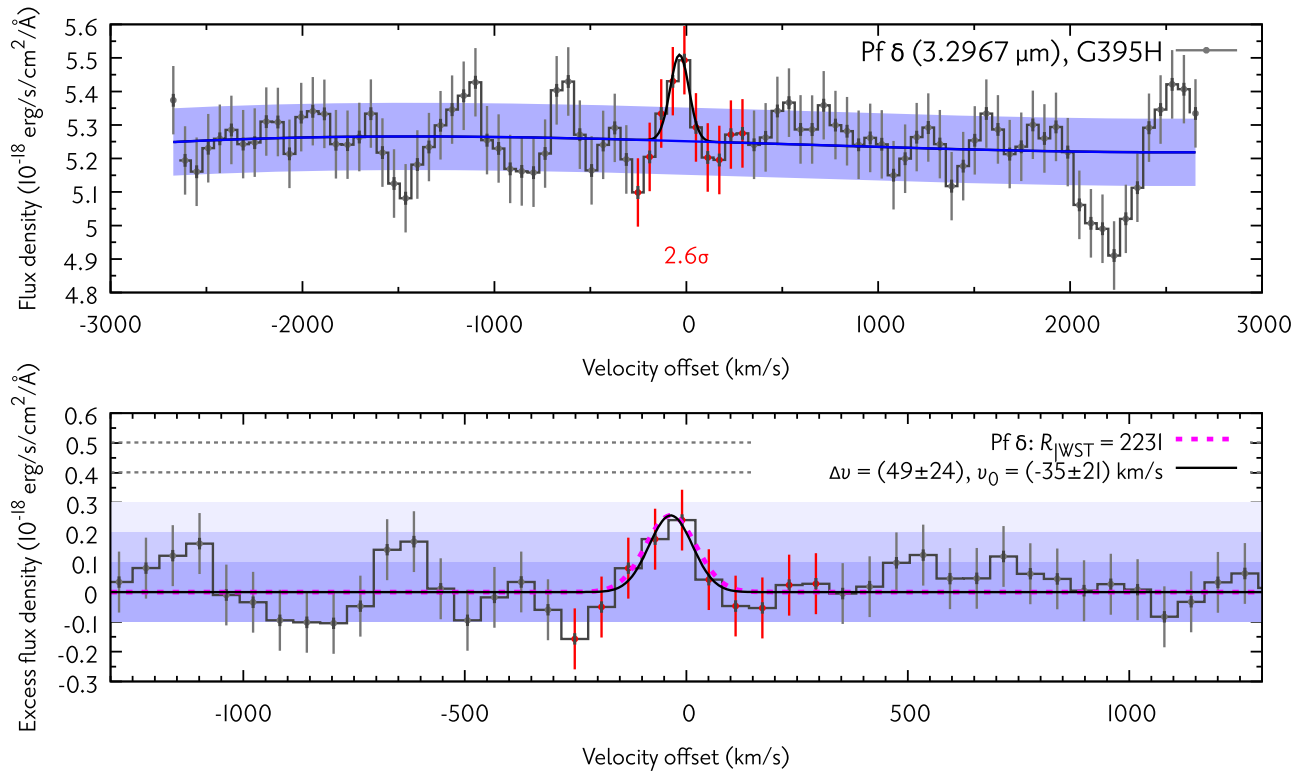
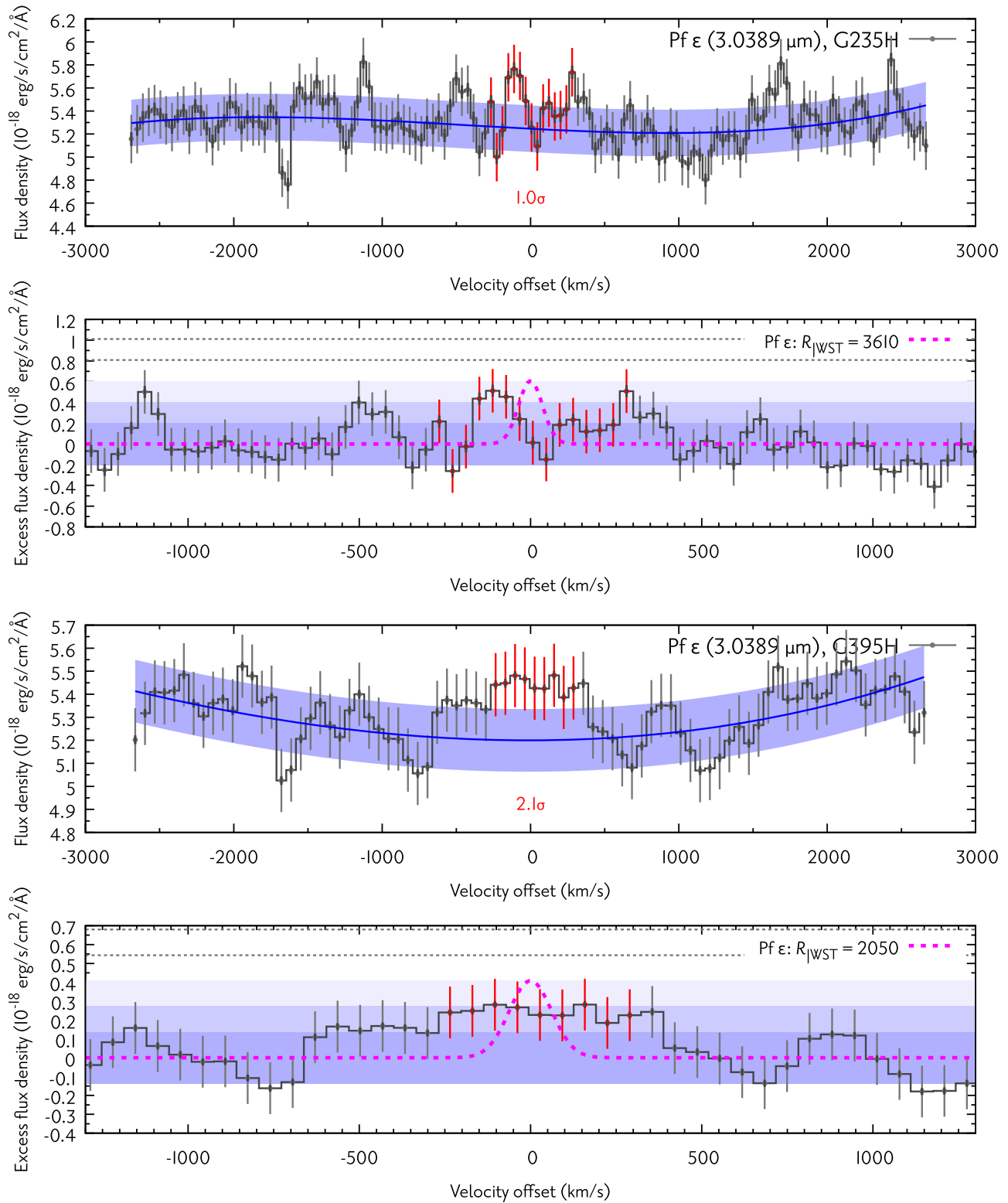**Figure 16.** As in Figure 15 but for Pfδ, very tentatively detected.

Figure 17. As in Figure 15 but for Pfε from two gratings (red half of G235H on top, blue half of G395H on the bottom), in both not detected.

ORCID iDs

Gabriel-Dominique Marleau ● https://orcid.org/0000-0002-2919-7500
Yuhiko Aoyama ● https://orcid.org/0000-0003-0568-9225
Jun Hashimoto ● https://orcid.org/0000-0002-3053-3575
Yifan Zhou ● https://orcid.org/0000-0003-2969-6040

References

Alcalá, J. M., Manara, C. F., Natta, A., et al. 2017, A&A, 600, A20
Alcalá, J. M., Natta, A., Manara, C. F., et al. 2014, A&A, 561, A2
Aoyama, Y., & Ikoma, M. 2019, ApJL, 885, L29
Aoyama, Y., Ikoma, M., & Tanigawa, T. 2018, ApJ, 866, 84
Aoyama, Y., Marleau, G.-D., Ikoma, M., & Mordasini, C. 2021, ApJL, 917, L30
Aoyama, Y., Marleau, G.-D., Mordasini, C., & Ikoma, M. 2020, arXiv:2011.06608
Bate, M. R. 2000, MNRAS, 314, 33
Betti, S. K., Follette, K. B., Ward-Duong, K., et al. 2022a, ApJL, 935, L18
Betti, S. K., Follette, K. B., Ward-Duong, K., et al. 2022b, ApJL, 941, L20
Betti, S. K., Follette, K. B., Ward-Duong, K., et al. 2023, AJ, 166, 262
Böker, T., Arribas, S., Lützgendorf, N., et al. 2022, A&A, 661, A82
Bonse, M. J., Garvin, E. O., Gebhard, T. D., et al. 2023, AJ, 166, 71
Bowler, B. P., Blunt, S. C., & Nielsen, E. L. 2020, AJ, 159, 63
Brittain, S. D., Najita, J. R., Dong, R., & Zhu, Z. 2020, ApJ, 895, 48
Calvet, N., & Gullbring, E. 1998, ApJ, 509, 802
Chauvin, G., Lagrange, A.-M., Dumas, C., et al. 2004, A&A, 425, L29
Demars, D., Bonnefoy, M., Dougados, C., et al. 2023, A&A, 676, A123
Eriksson, S. C., Asensio Torres, R., Janson, M., et al. 2020, A&A, 638, L6
Erkal, J., Manara, C. F., Schneider, P. C., et al. 2022, A&A, 666, A188
Faherty, J. K., Riedel, A. R., Cruz, K. L., et al. 2016, ApJS, 225, 10
Fischer, W., Kwan, J., Edwards, S., & Hillenbrand, L. 2008, ApJ, 687, 1117
Gaia Collaboration, Brown, A. G. A., Vallenari, A., et al. 2021, A&A, 649, A1
Gangi, M., Antoniucci, S., Biazzo, K., et al. 2022, A&A, 667, A124
Gardner, J. P., Mather, J. C., Abbott, R., et al. 2023, PASP, 135, 068001
Haffert, S. Y., Bohn, A. J., de Boer, J., et al. 2019, NatAs, 3, 749
Hartmann, L., Herczeg, G., & Calvet, N. 2016, ARA&A, 54, 135
Hasegawa, Y., Uyama, T., Hashimoto, J., et al. 2024, AJ, 167, 105
Herczeg, G. J., Chen, Y., Donati, J.-F., et al. 2023, ApJ, 956, 102
Herczeg, G. J., Cruz, K. L., & Hillenbrand, L. A. 2009, ApJ, 696, 1589
Herczeg, G. J., Wood, B. E., Linsky, J. L., Valenti, J. A., & Johns-Krull, C. M. 2004, ApJ, 607, 369
Jakobsen, P., Ferruit, P., Alves de Oliveira, C., et al. 2022, A&A, 661, A80
Jiaxuan, L. 2023, AstroJacobLi/smplotlib: v0.0.9, Zenodo, doi:10.5281/ZENODO.8126529
Komarova, O., & Fischer, W. J. 2020, RNAAS, 4, 6
Kwan, J., Edwards, S., & Fischer, W. 2007, ApJ, 657, 897
Lai, D., & Muñoz, D. J. 2023, ARA&A, 61, 517
Lodato, G., Delgado-Donate, E., & Clarke, C. J. 2005, MNRAS, 364, L91
Looper, D. L., Bochanski, J. J., Burgasser, A. J., et al. 2010, AJ, 140, 1486
Luhman, K. L. 2023, AJ, 165, 269
Luhman, K. L., Adame, L., D'Alessio, P., et al. 2007, ApJ, 666, 1219
Luhman, K. L., Tremblin, P., Birkmann, S. M., et al. 2023, ApJL, 949, L36
Lyons, L. 2013, arXiv:1310.1284
Manara, C. F., Frasca, A., Alcalá, J. M., et al. 2017, A&A, 605, A86
Manara, C. F., Testi, L., Rigliaco, E., et al. 2013, A&A, 551, A107
Marleau, G.-D., & Aoyama, Y. 2022, RNAAS, 6, 262
Marleau, G.-D., Aoyama, Y., Kuiper, R., et al. 2022, A&A, 657, A38
Marleau, G.-D., Kuiper, R., Béthune, W., & Mordasini, C. 2023, ApJ, 952, 89
Marois, C., Macintosh, B., Barman, T., et al. 2008, Sci, 322, 1348
Marois, C., Zuckerman, B., Konopacky, Q. M., Macintosh, B., & Barman, T. 2010, Natur, 468, 1080
Mohanty, S., Greaves, J., Mortlock, D., et al. 2013, ApJ, 773, 168
Mohanty, S., Jayawardhana, R., & Basri, G. 2005, ApJ, 626, 498
Mohanty, S., Jayawardhana, R., Huélamo, N., & Mamajek, E. 2007, ApJ, 657, 1064
Muñoz, D. J., Lai, D., Kratter, K., & Miranda, R. 2020, ApJ, 889, 114
Natta, A., Testi, L., Muzerolle, J., et al. 2004, A&A, 424, 603
Reggiani, M., Meyer, M. R., Chauvin, G., et al. 2016, A&A, 586, A147
Ricci, L., Cazzoletti, P., Czekala, I., et al. 2017, AJ, 154, 24
Ringqvist, S. C., Viswanath, G., Aoyama, Y., et al. 2023, A&A, 669, L12
Rodriguez, D. R., van der Plas, G., Kastner, J. H., et al. 2015, A&A, 582, L5
Salyk, C., Herczeg, G. J., Brown, J. M., et al. 2013, ApJ, 769, 21
Skemer, A. J., Close, L. M., Szűcs, L., et al. 2011, ApJ, 732, 107
Tanigawa, T., Ohtsuki, K., & Machida, M. N. 2012, ApJ, 747, 47
Thanathibodee, T., Calvet, N., Bae, J., Muzerolle, J., & Hernández, R. F. 2019, ApJ, 885, 94
Thanathibodee, T., Calvet, N., Hernández, J., Maucó, K., & Briceño, C. 2022, AJ, 163, 74
Theissen, C. A., Burgasser, A. J., Bardalez Gagliuffi, D. C., et al. 2018, ApJ, 853, 75
Theissen, C. A., West, A. A., Shippee, G., Burgasser, A. J., & Schmidt, S. J. 2017, AJ, 153, 92
Venuti, L., Stelzer, B., Alcalá, J. M., et al. 2019, A&A, 632, A46
Wagner, K., Follete, K. B., Close, L. M., et al. 2018, ApJL, 863, L8
Wagner, K., Stone, J., Skemer, A., et al. 2023, NatAs, 7, 1208
Wiese, W. L., & Fuhr, J. R. 2009, JPCRD, 38, 565